



LAWRENCE
LIVERMORE
NATIONAL
LABORATORY

High-resolution simulations and modeling of reshocked single-mode Richtmyer-Meshkov instability. I. Comparison to experimental data and to amplitude growth model predictions

M. Latini, O. Schilling, W. Don

May 18, 2006

Physics of Fluids

Disclaimer

This document was prepared as an account of work sponsored by an agency of the United States Government. Neither the United States Government nor the University of California nor any of their employees, makes any warranty, express or implied, or assumes any legal liability or responsibility for the accuracy, completeness, or usefulness of any information, apparatus, product, or process disclosed, or represents that its use would not infringe privately owned rights. Reference herein to any specific commercial product, process, or service by trade name, trademark, manufacturer, or otherwise, does not necessarily constitute or imply its endorsement, recommendation, or favoring by the United States Government or the University of California. The views and opinions of authors expressed herein do not necessarily state or reflect those of the United States Government or the University of California, and shall not be used for advertising or product endorsement purposes.

**High-resolution simulations and modeling of
reshocked single-mode Richtmyer-Meshkov instability.**

**I. Comparison to experimental data and to
amplitude growth model predictions**

Marco Latini*

*Applied and Computational Mathematics,
California Institute of Technology, Pasadena, California 91125*

Oleg Schilling†

*University of California, Lawrence Livermore
National Laboratory, Livermore, California 94551*

Wai Sun Don‡

Division of Applied Mathematics, Brown University, Providence, Rhode Island 02912

(Dated: May 13, 2006)

Abstract

The reshocked single-mode Richtmyer-Meshkov instability is simulated in two spatial dimensions using the fifth- and ninth-order weighted essentially non-oscillatory shock-capturing method with uniform spatial resolution of 256 points per initial perturbation wavelength. The initial conditions and computational domain are modeled after the single-mode, Mach 1.21 air(acetone)/SF₆ shock tube experiment of Collins and Jacobs [J. Fluid Mech. **464**, 113 (2002)]. The simulation densities are shown to be in very good agreement with the corrected experimental planar laser-induced fluorescence images at selected times before reshock of the evolving interface. Analytical, semi-analytical and phenomenological linear and nonlinear, impulsive, perturbation and potential flow models for single-mode Richtmyer-Meshkov unstable perturbation growth are summarized. The simulation amplitudes are shown to be in very good agreement with the experimental data and with the predictions of linear amplitude growth models for small times and with those of nonlinear amplitude growth models at later times up to the time at which the driver-based expansion in the experiment (but not present in the simulations or models) expands the layer before reshock. The qualitative and quantitative differences between the fifth- and ninth-order simulation results are discussed. Using a local and global quantitative metric, the prediction of the Zhang and Sohn [Phys. Fluids **9**, 1106 (1997)] nonlinear Padé model is shown to be in best overall agreement with the simulation amplitudes before reshock. The sensitivity of the amplitude growth model predictions to the initial growth rate from linear instability theory, the post-shock Atwood number and amplitude, and the velocity jump due to the passage of the shock through the interface is also investigated numerically. In Part II [Phys. Fluids (2006)], a comprehensive investigation of mixing induced by the reshocked single-mode Richtmyer-Meshkov instability is performed using the present simulation data to assess and quantify the effects of reshock and other waves on the mixing dynamics, including the post-reshock growth, circulation deposition, mixing profiles and fractions, baroclinic circulation deposition, energy spectra and statistics.

PACS numbers: 47.20.-k, 47.20.Ma, 47.20.Cq, 47.15.ki, 47.40.Nm, 47.40.-x, 47.11.Bc, 47.11.-j

*Electronic address: mlatini@acm.caltech.edu

†Author to whom correspondence should be addressed: schilling1@llnl.gov.

‡Electronic address: wsdon@cfm.brown.edu

I. INTRODUCTION

The Richtmyer-Meshkov instability occurs when perturbations on the interface separating two different fluids grow following the passage of a shock and eventually develop complex spatial structure. The instability derives its name from the linear instability analysis and numerical work of Richtmyer,¹ who considered the instability generated by a shock impulsively accelerating a sinusoidally-perturbed interface. The predictions of Richtmyer were subsequently confirmed in shock tube experiments performed by Meshkov.² This instability is of great fundamental interest in fluid dynamics,^{3,4} as well as of interest to inertial confinement fusion,⁵⁻⁸ supersonic combustion⁹ and supernovae dynamics.¹⁰⁻¹⁴ One of the challenges in understanding the Richtmyer-Meshkov instability is the accurate modeling of the growth of the mixing layer in the nonlinear phase and following reshock, as well as predicting the statistical properties and dynamics of turbulent mixing induced by this instability.

In the present work, the evolution of the classical Richtmyer-Meshkov instability in a model of the air (seeded with acetone) and sulfur hexafluoride (SF₆) Mach 1.21 experiment of Collins and Jacobs¹⁵ is investigated in two-dimensional planar geometry using the weighted essentially non-oscillatory (WENO) method (see Sec. II A for the equations solved and a brief description of the numerical method). As the shock passes through the material interface separating the air and acetone mixture [referred to as air(acetone) in the sequel] and the denser sulfur hexafluoride gas, the misalignment of the pressure and density gradients causes a deposition of vorticity through the baroclinic production mechanism. The vorticity evolution equation (shown here for three dimensions and in the absence of molecular dissipation terms)

$$\frac{d\boldsymbol{\omega}}{dt} = \frac{\nabla\rho \times \nabla p}{\rho^2} + \boldsymbol{\omega} \cdot \nabla\mathbf{u} - \boldsymbol{\omega} \nabla \cdot \mathbf{u} \quad (1)$$

describes the dynamics of vorticity generation, where $d/dt = \partial/\partial t + \mathbf{u} \cdot \nabla$ is the convective derivative, $\boldsymbol{\omega} = \nabla \times \mathbf{u}$ is the vorticity, \mathbf{u} is the velocity, ρ is the density and p is the pressure. The first term on the right side is the baroclinic production term, and constitutes the principal mechanism of vorticity generation by the Richtmyer-Meshkov instability. In particular, this term is large when a shock passes through the interface and when waves interact with the interface. The second term on the right side is the vortex-stretching term (which is zero in the present two-dimensional investigation, as the vorticity and velocity fields are orthogonal). This term enhances dissipation, resulting in more diffuse and smaller

scale structures in three-dimensional turbulence. The third term on the right side is the compression term, and does not contribute significantly to the vorticity evolution. Following the passage of the shock, the perturbed interface is set in motion along the direction of shock propagation, a reflected shock returns back into the air(acetone) gas, and a transmitted shock enters the SF₆ gas. The vorticity baroclinically deposited on the interface by the shock drives the evolution of the instability, with spikes of the heavier fluid (SF₆) penetrating the lighter fluid [air(acetone)] and bubbles of the lighter fluid “rising” in the heavier fluid. At late times, the vorticity coalesces into strong cores, causing the mushroom roll-ups characteristic of the Richtmyer-Meshkov instability. When the fluids are miscible, molecular mixing occurs between these interpenetrating fluids, generating a mixing layer and a topologically-complex interface. In the present investigation, explicit molecular mixing is not modeled; instead, numerical diffusion across the interface models the ‘mixing’ process.

Additional vorticity deposition and enhanced mixing occur in the configuration considered here, in which the transmitted shock from the initial shock-interface interaction reflects elastically from the end wall of the shock tube test section and interacts with the evolving layer. This second interaction (referred to as *reshock*) deposits vorticity of opposite sign so that bubbles transform into spikes and vice versa in a process called *inversion*. The inversion induces the formation of additional complex structure, with more disorganized small-scale flow features observed at late times. Following reshock, the interface changes its direction of motion and moves away from the end wall of the test section: a transmitted shock enters the air(acetone) and a reflected rarefaction returns into the SF₆. The rarefaction wave is reflected from the end wall of the test section and interacts with the evolving interface, again resulting in the formation of additional complex, small-scale structures.

Throughout the instability evolution, both prior to and following reshock, additional vortex-accelerated secondary baroclinic vorticity is deposited on the interface^{3,16}, where the vorticity is generated by the misalignment between the density gradient and the centripetal acceleration of the cores $\nabla p \times \nabla \rho \sim -\rho \mathbf{u}/dt \times \nabla \rho$. This secondary instability further enhances the development of a complex interface topology (with increasing length in two dimensions and surface area in three dimensions), eventually resulting in a mixing layer that becomes turbulent at sufficiently large Reynolds numbers.¹⁷ The reshocked single-mode Richtmyer-Meshkov instability is considered in the present work to investigate two phases of the instability development and their coupling: the linear and nonlinear phases prior to

reshock (Part I), and the post-reshock and late-time (quasi)-decay phases (Part II).

To our knowledge, *the present work is the first comprehensive application of the WENO method to the study of the classical reshocked Richtmyer-Meshkov instability.* The vast majority of numerical simulations and experiments on single- and multi-mode Richtmyer-Meshkov instabilities to date have considered the flow evolution initiated by only a single shock-interface interaction. Mikaelian¹⁸ performed arbitrary Lagrangian-Eulerian simulations of gas configurations consisting of three layers, 1/2/1, with fluid 1 representing semi-infinite air layers and fluid 2 representing a finite-thickness freon, SF₆, or helium layer, having perturbations either on the upstream or downstream side. The shock Mach number was 1.5. These simulations investigated freeze-out, interface coupling and feedthrough. Sadot *et al.*¹⁹ found very good agreement between the amplitude growth from their single-mode reshocked Richtmyer-Meshkov instability experiment and numerical simulation data prior to the arrival of the rarefaction wave from the end wall. As in the case of experiments, the quantitative data obtained from these simulations was mainly limited to the consideration of perturbation amplitude growth. Numerical studies of the single-mode impulsive Richtmyer-Meshkov instability experiment with reshock of Jacobs, Jones and Niederhaus^{20,21} were performed by Kotelnikov and Zabusky²² and Kotelnikov, Ray and Zabusky²³ using the vortex-in-cell method and the contour advection semi-Lagrangian method (n.b., the Jacobs *et al.*²⁴ and Rightley *et al.*²⁵ Mach 1.2 experiment with reshock was also simulated using a Godunov method²³). Kremeyer *et al.*²⁶ used a fifth-order WENO method to simulate the Richtmyer-Meshkov instability in a shock tube containing gases with different initial transverse density profiles to investigate shock splitting and, in particular, the role of shock bowing and vorticity dynamics. Top-hat shaped perturbations, including those shaped as a notch, were considered instead of a sinusoidal perturbation considered in classical investigations of this instability. Zhang *et al.*²⁷ simulated the interactions between planar Mach 1.095 and 1.2 shocks and an SF₆ gas cylinder using the fifth- and seventh-order WENO method, and qualitatively and quantitatively studied the mechanisms of baroclinic vorticity and circulation generation. All of the above simulations were two-dimensional.

This paper is organized as follows. The equations solved and a summary of the WENO method are presented in Sec. IIA. The initial conditions and computational domain adapted from the Mach 1.21 experiment of Collins and Jacobs¹⁵ are specified in Sec. IIB. Simulations of the reshocked single-mode Richtmyer-Meshkov instability using the fifth- and ninth-order

WENO method are presented and discussed in Sec. IIC. The density evolution is compared to the corrected experimental PLIF images of Collins and Jacobs before and after reshock in Sec. IID. A review of the principal linear and nonlinear models for single-mode perturbation amplitude growth is presented in Sec. III, including the most widely used impulsive, perturbation and potential flow models. The simulation amplitudes before reshock are compared to the experimental data and to the model predictions in Sec. IV. Finally, the sensitivity of the amplitude growth model predictions to the parameters entering into the models (the initial linear growth rate, the post-shock Atwood number, the post-shock amplitude and the velocity jump due to the passage of the shock through the interface) is explored by self-consistently comparing the predictions using numerically and experimentally determined values of these parameters. A summary of the results and conclusions are given in Sec. V.

In Part II, a comprehensive investigation of the dynamics of the mixing process induced by the reshocked Richtmyer-Meshkov instability, and more generally by complex hydrodynamic shock-driven flows, is presented. The methods used are adapted from classical investigations of turbulence and turbulent mixing, and synthesize high-resolution numerical simulation data, theoretical models for instability growth, and available experimental data. The reshock process is qualitatively described using simulated density Schlieren images and other fields. The post-reshock simulation amplitudes are compared to the predictions of several models for the growth of a reshocked interface. The time-evolution of various mixing quantities is investigated, including mole fraction profiles, production fractions, mixing fractions, energy spectra and statistics. The effects of reshock on these quantities is explored. Finally, the effects of the reflected rarefaction and other waves following reshock on the flow is considered. This investigation suggests that a variety of quantities should be considered to more completely characterize the mixing layer dynamics.

The key new contributions to better understanding the physics of the two-dimensional reshocked Richtmyer-Meshkov instability presented in Parts I and II are: (1) the first comprehensive simulation of the Richtmyer-Meshkov instability with reshock using the fifth- and ninth-order WENO method; (2) a comprehensive survey of a wide range of amplitude growth models and a summary of their derivations and phenomenology to investigate the nonlinear phase of this instability; (3) direct qualitative and quantitative comparisons of simulation data to experimental data (thus providing an element of validation of the numerical methods as used here) and discussing the differences between the fifth- and ninth-order

WENO results; (4) a comprehensive application of all of the amplitude growth models to one experimental and simulation dataset (also with the bubble and spike amplitudes obtained separately by performing an unperturbed simulation); (5) a sensitivity study to emphasize that small differences in the amplitude model parameters can affect the model predictions; (6) a detailed qualitative examination of the reshock process, including consideration of the simulated density Schlierens and baroclinic vorticity production fields to examine the structure internal to the roll-up and of the post-reshock flow; (7) a comparison of the simulation data to the predictions of three existing post-reshock growth models; (8) computation, discussion and interpretation of a wide range of quantities that have been used to characterize other mixing layers (not considered in previous work applied to this instability); (9) a comparison of many of the above quantities just after and before reshock, to quantitatively assess the effects of reshock, and; (10) a novel investigation of the role of wave-interface interactions on the above quantities by comparing them for reflecting and outflow boundary conditions at the end wall.

II. HIGH-RESOLUTION SIMULATIONS OF TWO-DIMENSIONAL RESHOCKED SINGLE-MODE RICHTMYER-MESHKOV INSTABILITY

In this section, weighted essentially non-oscillatory (WENO) shock-capturing simulations of two-dimensional reshocked single-mode Richtmyer-Meshkov instability are described. The WENO method is a modern high-resolution reconstruction-evolution shock-capturing method^{28,29} used for the simulation of compressible turbulent flows. As the numerical algorithm is based on the discretization of the Euler equations, the truncation errors can be regarded as an implicit nonlinear high-order numerical dissipation, i.e., no explicit artificial viscosity or filtering to suppress Gibbs oscillations is required. As the non-dissipative compressible fluid dynamics equations are formally ill-posed,³⁰ this numerical dissipation regularizes the numerical scheme and renders the method stable. Formally higher-order numerical flux reconstructions are less dissipative than lower-order reconstructions. It is important to appreciate that flows with shocks cannot be modeled using direct numerical simulation (DNS), and are therefore presently modeled using numerically dissipative shock-capturing schemes, monotone-integrated large-eddy simulations³¹ (MILES) or implicit large-eddy simulations³² (ILES). It is also important to appreciate that two-dimensional sim-

ulations can achieve much higher resolutions than can be obtained in three dimensions using the same computational resources.

A. Equations solved and the WENO method

The characteristics-based weighted essentially non-oscillatory (WENO) scheme in the conservative finite-difference formulation^{33,34} is used in the present investigation. The Euler equations are augmented by the equation for mass fraction conservation of the second gas (SF_6) in order to track the interface and mixing: in two dimensions

$$\frac{\partial}{\partial t} \begin{bmatrix} \rho \\ \rho u \\ \rho v \\ \rho e \\ \rho m \end{bmatrix} + \frac{\partial}{\partial x} \begin{bmatrix} \rho u \\ \rho u^2 + p \\ \rho u v \\ (\rho e + p) u \\ \rho m u \end{bmatrix} + \frac{\partial}{\partial y} \begin{bmatrix} \rho v \\ \rho u v \\ \rho v^2 + p \\ (\rho e + p) v \\ \rho m v \end{bmatrix} = 0, \quad (2)$$

where ρ is the density, $\mathbf{u} = (u, v)$ is the velocity, p is the pressure, $e = (u^2 + v^2)/2 + U$ is the total (kinetic plus internal) energy per unit mass, $U = p/(\gamma - 1)$ is the internal energy, $p = \rho RT$ is the ideal gamma law gas pressure (R is the universal gas constant) and m is the mass fraction (here of SF_6). In the present simulations, a single-gamma is used as multiple gammas create non-physical pressure oscillations near the material interfaces (which are non-trivial to mitigate) in conservative shock-capturing schemes for the multi-component fluid equations.^{35–38} The fifth- and ninth-order simulations were identical in every respect except for the reconstruction order.

A conservative finite-difference formulation for hyperbolic conservation laws requires consistent high-order numerical fluxes at the cell boundaries in order to construct the flux difference across the uniformly-spaced cells. For the Euler equations, the eigensystem of fluxes is obtained from the Jacobian of the Roe-averaged fluxes in each spatial dimension. Lax-Friedrichs flux-splitting is used to split the original fluxes into their positive and negative components (with an introduction of additional artificial dissipation in order to obtain smoother fluxes³³). The resulting positive and negative flux components are then projected in the characteristic fields using the left eigenvectors to form the positive and negative characteristic variables at each cell center. Then, WENO polynomial reconstruction is used to reconstruct the fluxes at the cell boundaries with high-order of accuracy: a weighted convex

combination of all possible r th degree piecewise-polynomial approximations (e.g., $r = 3$ for fifth-order and $r = 5$ for ninth-order) of the characteristic variables using the neighboring cell-centered values is constructed and evaluated at the boundaries of a given cell. For a given order of reconstruction, there are r possible r th-degree piecewise-polynomials available, with smoothness properties depending on the smoothness of the underlying solution. The essential element of WENO reconstruction is an adaptive nonlinear assignment of the weights given to those r polynomials: the weight is designed such that a polynomial of degree $2r - 1$ is formed for the locally-smooth regions of the solution and an essentially non-oscillatory lower r th-degree polynomial (i.e., upwinding) is used otherwise to avoid Gibbs oscillations when approximating solution discontinuities. The weights of the r choices of possible stencils around a given cell center are computed utilizing the properly scaled local gradient and curvature of the data via a divided difference. Hence, relatively smaller (or close to zero) weights are assigned to polynomials approximating the discontinuous data and nearly equal weights are assigned to polynomials approximating the smooth data. The high-order reconstructed positive and negative characteristic variables are summed and then projected back to physical space via the right eigenvectors, forming a high-order numerical flux at the cell boundaries. The *formal* spatial order of accuracy of the scheme is $2r - 1$ in smooth flow regions. As for *all* other numerical methods, the actual computational accuracy diminishes to at best first-order near the shock. Although the global order of the solution is reduced to first near a shock, the high-order reconstruction yields an efficient high-resolution algorithm, which is essential to long-time, multi-scale simulations of complex shock-induced flows. In the present study, the semi-discrete equations are evolved in time using the third-order total variation diminishing (TVD) Runge-Kutta scheme.³⁹

The WENO code used here provides a framework for the multi-dimensional numerical simulation of the fully-nonlinear evolution of hydrodynamic instabilities and late-time mixing generated by single- and multi-mode Richtmyer-Meshkov, Rayleigh-Taylor and Kelvin-Helmholtz instabilities. The nonlinear system of hyperbolic partial differential equations can be solved in one, two or three spatial dimensions. Although fifth- and ninth-order flux reconstructions are used presently, other odd orders of WENO polynomial reconstruction can be specified, including third-, seventh- and eleventh-order.

B. Description of the Mach 1.21 experiment of Collins and Jacobs

The initial conditions for the present simulations were adapted from the Mach 1.21 shock tube experiment of Collins and Jacobs.¹⁵ This experiment was selected for comparison of the numerical results to the high-resolution corrected density planar laser-induced fluorescence (PLIF) images showing the evolution of the instability and to the measured perturbation amplitude prior to reshock. The experiment was performed in a vertical shock tube using a novel technique to generate a membraneless perturbed interface. The shock tube had a square test section with cross-section $8.9 \text{ cm} \times 8.9 \text{ cm}$ and length 75 cm. The driver section had a diameter of 10.2 cm and length 100 cm (with a mixture of 50% air and 50% N_2), and the driven section has a cross-section of $8.9 \text{ cm} \times 8.9 \text{ cm}$ and length of 261 cm (n.b., these dimensions are specified more accurately than originally reported by Collins and Jacobs.¹⁵). The shock was generated through the rupture of a diaphragm and propagated into a mixture of 75% air and 25% acetone by volume at standard room temperature and pressure. The shock then refracted at the perturbed interface separating the air(acetone) mixture and the denser sulfur hexafluoride (SF_6) gas, giving rise to the growth and evolution of the Richtmyer-Meshkov instability.

The membraneless interface was generated as follows.⁴⁰ The shock tube contained horizontal slots on the two opposite walls. The gases entered the shock tube from the opposite ends, flowed toward each other, and exited through the two slots, resulting in a fine, initially diffuse interface separating the air(acetone) and SF_6 . A sinusoidal perturbation was then generated by gently oscillating the vertical shock tube horizontally using an eccentric stepper motor at a prescribed frequency to establish a standing wave. The initial diffuse interface was estimated to be $\approx 0.5 \text{ cm}$ wide using the maximum slope determined by the measurement of the acetone concentration. PLIF was used to visualize the instability evolution using a mixture of the fluorescent acetone with air. The PLIF images were corrected for non-uniform laser illumination and Beer's law attenuation. A set of experiments was conducted for shocks with Mach numbers 1.21 ± 0.02 , and images were captured up to 11 ms following the initial shock-interface interaction. The evolution of the instability, with spikes of heavier fluid penetrating the lighter fluid and bubbles of lighter fluid "rising" in the heavier fluid, was investigated. The reshock phase when the transmitted shock reflected from the end wall of the test section and interacted with the evolving interface was also

described. Concurrent with the arrival of the reflected shock, a reflected rarefaction wave also interacted with the interface. This initial rarefaction wave (referred to as the *driver-based expansion wave* in the sequel) was created by the rupture of the membrane generating the initial shock; this wave was subsequently reflected from the end (top) wall of the shock tube, and then interacted with the interface. This interaction with the reflected rarefaction formed additional complex structure on the evolving interface.

C. Description of the simulations

In the present simulations, only the shock tube test section is considered, so that the driver-based expansion wave is not captured numerically. Furthermore, the effects of gravity and the horizontal motion of the shock tube are neglected. The upstream conditions were matched in order to specify a single value of the adiabatic exponent, $\gamma = 1.24815$, corresponding to the air(acetone) mixture. The thermodynamic properties of air(acetone) vapor and SF₆, including differences between the single-gamma simulations and the conditions that *would be obtained* if two gammas were used are given in Table I (where some quantities were obtained using one-dimensional shock refraction theory). Reshock occurs ≈ 0.25 ms earlier in the present simulations than would occur in two-gamma simulations.

To match the shock tube test section dimensions, the computational domain had (x, y) dimension $[0, L_x] \times [0, L_y]$ with $L_x = 78$ cm, $L_y = 8.9$ cm, and centerline of the perturbed initial interface located at $x = 3$ cm. The shock is initiated at $x = 1$ cm using the Rankine-Hugoniot conditions corresponding to a $Ma = 1.21$ shock in the air(acetone). The simulations had a grid resolution $\Delta x = \Delta y = 0.0232$ cm corresponding to 256 points per initial perturbation wave length. A CFL number of 0.45 was used.

As in the experiment, the sinusoidal interfacial perturbation in the simulations $\eta(y) = a_0 \sin(ky)$ had amplitude $a_0 = 0.2$ cm (slightly larger than the mean value 0.183 cm reported in the experiment) to better match the post-shock amplitude, perturbation wave length $\lambda = 5.93333$ cm, and diffuse interface width $\delta = 0.5$ cm. Thus, $ka_0 = 0.21 \ll 1$, where $k = 2\pi/\lambda$ is the perturbation wave number, so that the initial growth is linear.

The boundary conditions were: (1) *inflow at the entrance of the test section* in the streamwise (x) direction; (2) *reflecting at the end wall of the test section* in the streamwise direction, and; (3) *symmetry in the spanwise (y) direction* corresponding to the cross-section of the test

section. Any turbulent boundary layers on the side walls or other molecular viscous/diffusive effects present in the experiment are not captured in these inviscid simulations.

In the current investigation, where the computed fluid dynamic fields remain unchanged over large regions of the domain until late times, a novel adaptive domain algorithm automatically enlarged the domain size along the shock propagation direction, when changes from the constant state were detected. This allowed the simulation to begin with a smaller domain of length $L_x = 9.3472$ cm, corresponding to a streamwise resolution of $N_x = 407$. When the algorithm detected changes in a designated quantity (such as density in the present case), as the shock or disturbances arrived near the downstream shortened domain boundary, the domain size was enlarged by 3 cm until the end of the domain was reached at $L_x = 78$ cm, corresponding to a final resolution of $N_x = 3372$.

D. Qualitative comparison of density evolution to experimental PLIF images

Corrected PLIF density images from the Collins and Jacobs Mach 1.21 shock tube experiment are compared to the simulation density fields in Fig. 1 at selected times (2.5, 3, 4 and 5 ms) *before reshock*: the experimental images are shown in the middle row and the fields from the ninth- and fifth-order simulation are shown in the top and bottom row, respectively (n.b., the simulation fields are rotated 90° counterclockwise in Figs. 1–3 to facilitate comparison with the experimental images). The PLIF images are shown in false color, with red and blue corresponding to the lowest and highest fluorescent intensity, respectively. The temporal sequence of images was obtained from an ensemble of highly reproducible shock tube experiments. In general, the numerical and experimental images are in very good qualitative agreement. By 5 ms, a well-formed mushroom roll-up forms with entrainment of the air(acetone) into the vortex core. Small differences in the width of the mushroom ‘stem’ and the width of the ‘cap’ can be observed between the experiment and the simulations. The experimental images show more pronounced structure inside the vortex roll-ups, and the roll-ups in the simulations are more spatially compact than those in the experiment. The ninth-order simulation captures more of the roll-up structure observed in the experiment at late times than does the fifth-order simulation.

The comparison of the experimental PLIF images to the simulation densities is continued in Fig. 2 at times just before and *following reshock* (6, 6.58 and 6.88 ms). The ninth-order

simulation captures the secondary instability within the roll-ups at 6 ms. The simulation densities at 6.58 and 6.88 ms exhibit the wave structure developing at the interface as the transmitted shock enters the air(acetone) gas and the reflected rarefaction returns into the SF₆. A progressively larger time delay reaching ≈ 1 ms develops by 6.88 ms as the simulations lag in time behind the PLIF density images. This time delay can be explained by the arrival of the driver-based expansion wave in the experiment (which decelerates the evolving interface), as well as by the difference in the interface velocity between the simulation and experiment. The rarefaction also causes the formation of small-scale structures on the interface that are amplified during reshock. The experimental image shows increased mixing and fragmentation of large structures at 7.781 ms: this results from the excitation of fluctuations in the third spatial dimension caused by the driver-based expansion wave present in the experiment and subsequently amplified by reshock (which is not captured in the simulations), as well as of other excitation mechanisms that may be present. The simulations show that more complex, finer and disordered structures form following reshock. In addition, the ninth-order simulation shows the appearance of small-scale roll-ups on the fluid interface that are not present in the experimental and fifth-order simulation images. This may be due to molecular dissipation effects present in the experiment, and to the numerical dissipation in the fifth-order simulation that is significantly larger than that in the ninth-order simulation. Note that the PLIF images in Figs. 1 and 2 exhibit boundary layer effects on the left side wall that are not present in the simulations.

A close-up of the roll-ups, including a comparison of the internal structure from the fifth- and ninth-order simulations is shown in Fig. 3 at 4, 5, 6 and 6.38 ms. The large-scale features are similar between the simulations. The ninth-order simulation densities exhibit sharper roll-ups and include more complex internal corrugated structure than the fifth-order densities. The additional structure within the roll-up has been attributed to the vortex-accelerated secondary baroclinic circulation,¹⁶ which causes vorticity of opposite sign to appear inside the core, contributing to additional mixing and to fragmentation. Such structures have also been observed in the recently reported late-time, single-mode Richtmyer-Meshkov instability experiments of Jacobs and Krivets.⁴¹ See Part II for further discussion of the structure in the roll-up, including the effects of reshock.

The qualitative comparison above shows that it is possible to achieve very good agreement between a two-dimensional, high-resolution shock-capturing simulation with high-order

WENO flux reconstruction and experimental density PLIF images *before reshock when three-dimensional effects are not significant*. In addition, the comparison of the densities from the fifth- and ninth-order simulations at 5 and 6 ms demonstrates that higher-order reconstruction better captures secondary instabilities on the interface and within the vortex cores. The roll-ups in the ninth-order simulation appear tighter and sharper, and with more fine-scale structure. The numerical simulation fields also display the shock focusing during the reshock process (see Part II for a more detailed examination of this process).

Following reshock, the experiment and simulations exhibit distinctively different flow structures due to the absence of the driver-based expansion wave and the increased importance of three-dimensional effects (including vortex stretching and associated mechanisms) that are not accounted for in the present simulations. This results in the formation and persistence of large-scale structures in the simulations, consistent with the inverse cascade of kinetic energy from small scales to larger scales in two-dimensional turbulence experiments and simulations, and explains the much larger simulation amplitudes following reshock compared to the experimental data points (further discussed in Part II). The experiments are affected by molecular diffusion and dissipation mechanisms which are not explicitly modeled by the equations solved numerically, i.e., the simulations contain implicit numerical diffusion and dissipation that may not be comparable to the molecular values in the physical experiment. The comparison of the fifth- and ninth-order simulations shows that as the order is increased, finer and more complex asymmetric structures appear, consistent with a reduced level of numerical dissipation. The sensitivity of the results to third-, fifth- and ninth-order spatial flux reconstruction, to grid resolution corresponding to 128, 256 and 512 points per initial perturbation wave length, and to numerical dissipation are systematically and self-consistently examined elsewhere.

III. LINEAR AND NONLINEAR PERTURBATION AMPLITUDE GROWTH MODELS

The prediction of the Richtmyer-Meshkov instability growth in the weakly-nonlinear, nonlinear and turbulent regimes is of contemporary interest.^{3,4} An overview of the principal perturbation amplitude growth models categorized according to their underlying physical assumptions on the flow is presented in this section. It is implicitly assumed in these

models that molecular dissipation and diffusion effects, surface tension, and other effects are negligible (extensions of some of the models to include such effects have been developed, but are not discussed here). While each of these models has limitations and a restricted domain of applicability, they represent an effort to better understand fundamental aspects of Richtmyer-Meshkov instability growth into the nonlinear regime.

The definitions of the bubble and spike amplitudes $a_b(t)$ and $a_s(t)$, and the mixing layer width $h(t)$ are illustrated in Fig. 4. The contour shows the canonical early-time evolution of the interface induced by the Richtmyer-Meshkov instability from a sinusoidal initial perturbation. The spikes penetrate into the lighter fluid and roll up, while bubbles “rise” into the heavier fluid. The solid horizontal line shows the location of the shocked, unperturbed interface used as a reference for the determination of the bubble and spike amplitudes from the simulation data. The distance from the unperturbed interface to the bubble tip is the bubble amplitude a_b , while the distance from the unperturbed interface to the spike tip is the spike amplitude a_s . The numerical determination of these amplitudes is discussed in Sec. IVA. The *mixing layer width* is the sum of the bubble and spike amplitudes

$$h(t) = a_b(t) + a_s(t). \quad (3)$$

The *mixing layer amplitude* predicted by the models presented in this section is the average of the bubble and spike amplitude

$$a(t) = \frac{a_b(t) + a_s(t)}{2}, \quad (4)$$

i.e., one-half the mixing layer width. The corresponding *mixing layer width and amplitude growth rates* are $dh/dt = da_b/dt + da_s/dt$ and $da/dt = (da_b/dt + da_s/dt)/2$, respectively. Each of the models for da/dt considered below can be integrated analytically to obtain $a(t)$. The corresponding bubble and spike (tip) velocities used in Sec. IVC are $v_b(t) = da_b/dt$ and $v_s(t) = da_s/dt$, respectively.

For the model summary given below, it is useful to define the key quantities appearing in the models: $k = 2\pi/\lambda$ is the wave number of the initial perturbation (where λ is the initial perturbation wave length), a_0^- is the pre-shock initial perturbation amplitude, a_0^+ is the post-shock initial perturbation amplitude, $A^- = (\rho_1^- - \rho_2^-)/(\rho_1^- + \rho_2^-)$ is the pre-shock Atwood number, $A^+ = (\rho_1^+ - \rho_2^+)/(\rho_1^+ + \rho_2^+)$ is the post-shock Atwood number, and Δu is the velocity jump at the interface following shock refraction. In some of the definitions of

the models, the scalings

$$\tau = k v_0 t \quad , \quad v_0 = k \Delta u A^+ a_0^+ \quad (5)$$

are used, where v_0 is the Richtmyer velocity.

A. Impulsive models

Impulsive models based on representing the shock as an instantaneous δ -function acceleration are briefly reviewed and summarized here. Impulsive models for the Richtmyer-Meshkov instability were developed by adapting existing models for the Rayleigh-Taylor instability (subject to a constant acceleration) to the case of an impulsive acceleration. These models predict a linear growth in time of the perturbation amplitude that captures the early stages of the instability evolution before nonlinear saturation effects become dominant.

1. The Richtmyer model

The first impulsive model proposed for the growth of a single-mode perturbation is due to Richtmyer.¹ Richtmyer modified earlier work⁴² on the growth of a small single-mode perturbation with amplitude $a(t)$ and wave number k when a dense fluid is accelerated continuously into a lighter fluid [the Rayleigh-Taylor instability described by $d^2a/dt^2 = gAk$ with $A = (\rho_1 - \rho_2)/(\rho_1 + \rho_2)$ the Atwood number], by replacing the constant gravitational acceleration g with an impulsive acceleration $\Delta u \delta(t)$:

$$\frac{da}{dt} = k \Delta u A^+ a_0^+ \equiv v_0 . \quad (6)$$

Integrating gives

$$a(t) = (1 + k \Delta u A^+ t) a_0^+ . \quad (7)$$

2. The Meyer-Blewett model

Meyer and Blewett⁴³ performed two-dimensional Lagrangian simulations of the single-mode Richtmyer-Meshkov instability and computed growth rates corresponding to a shock propagating from a light to a heavy gas and vice versa. Good agreement with the Richtmyer formula, Eq. (6), was obtained for the light-to-heavy case; however, better agreement in the

heavy-to-light case than that given by Eq. (6) was obtained by averaging the pre- and post-shock amplitudes,

$$\frac{da}{dt} = k \Delta u A^+ \frac{a_0^+ + a_0^-}{2}. \quad (8)$$

Integrating gives

$$a(t) = a_0^+ + k \Delta u A^+ \frac{a_0^+ + a_0^-}{2} t. \quad (9)$$

3. The Fraley model

Fraley⁴⁴ presented an analytic solution to the linearized perturbation equations in the case of a reflected shock wave. The complete set of linearized, compressible perturbation equations was first solved numerically by Richtmyer.¹ Fraley reconsidered the perturbation equations for a single-mode initial perturbation and solved them using Laplace transform techniques in the time domain. For weak shocks the solution is given by (see Ref. 4)

$$\frac{da}{dt} = k \Delta u a_0^- \left[A^- + \epsilon \frac{F(c, A^-)}{\gamma_1} \right], \quad (10)$$

where $\epsilon = 1 - p^-/p^+$ is the shock strength, $F(c, A^-) \equiv \left\{ \frac{(c-1)^2}{2} - \frac{1+A^-}{1-A^-} - c + \frac{1}{c} \left[\frac{(1+A^-)^2}{1-A^-} + (1-A^-) c^2 \right] \right\} \frac{1-A^-}{c+1}$, $c \equiv \sqrt{(1+A^-) \gamma_2 / (1-A^-) \gamma_1}$, and γ_1 and γ_2 are the adiabatic exponents of the ideal gases to the left and right of the interface, respectively. Integrating Eq. (10) gives

$$a(t) = a_0^+ + k \Delta u \left[A^- + \epsilon \frac{F(c, A^-)}{\gamma_1} \right] t a_0^-. \quad (11)$$

The Fraley solution was first recognized by Mikaelian⁴⁵ as the most accurate solution for the initial perturbation growth.

4. The Vandenboomgaerde-Mügler-Gauthier model

Vandenboomgaerde, Mügler and Gauthier⁴⁶ modified the Richtmyer model by replacing the impulsive acceleration, post-shock Atwood number and post-shock amplitude with linearly time-varying values from pre- to post-shock quantities, obtaining

$$\frac{da}{dt} = k \Delta u \left[\frac{A^+ a_0^+ + A^- a_0^-}{2} - \frac{(A^+ - A^-)(a_0^+ - a_0^-)}{6} \right]. \quad (12)$$

In applications of this formula, the second term on the right is typically very small compared to the first term and is neglected. Integrating Eq. (12) gives

$$a(t) = a_0^- + k \Delta u \left[\frac{A^+ a_0^+ + A^- a_0^-}{2} - \frac{(A^+ - A^-)(a_0^+ - a_0^-)}{6} \right] t. \quad (13)$$

5. The Mikaelian model for diffuse interfaces

Mikaelian⁴⁷ extended the work of Duff, Harlow and Hirt⁴⁸ for diffuse interfaces in the Rayleigh-Taylor instability to the Richtmyer-Meshkov instability, obtaining

$$\frac{da}{dt} = \frac{k \Delta u A^+}{\psi^+} a_0^+, \quad (14)$$

where ψ^+ is the growth reduction factor (in general, a function of a and A^+) satisfying the eigenvalue equation $\frac{d}{dx}(\rho \frac{df}{dx}) = \left(\rho - \frac{\psi^+}{k A^+ \Delta u} \frac{df}{dx} \right) k^2 f$. This equation was solved assuming a density profile of the form $\rho(x) = \bar{\rho} [1 + A^+ \tanh(x/\delta)]$ or $\rho(x) = \bar{\rho} [1 + A^+ \operatorname{erf}(x/\delta)]$, where $\bar{\rho} = (\rho_1 + \rho_2)/2$, so that the change in density occurs over a diffuse interface width δ . Integrating Eq. (14) gives

$$a(t) = \left(1 + \frac{k \Delta u A^+}{\psi^+} t \right) a_0^+. \quad (15)$$

B. Perturbation models

Models based on the asymptotic expansion of the linear perturbation equations are briefly reviewed here. These models generate asymptotic series with limited radii of convergence: the convergence can be improved using Padé approximants.

1. The Zhang-Sohn model

Zhang and Sohn⁴⁹ developed a model for the growth of a two-dimensional Richtmyer-Meshkov unstable interface from early to late times in the case of a reflected shock (light-to-heavy transition). The dynamics of the interface are modeled using the linear, compressible flow equations for early times and using the nonlinear, incompressible flow equations for later times. Let $y = \eta(x, t)$ denote the initial perturbation and let $\phi_r(x, y, t)$ denote the velocity potentials of the inviscid, irrotational fluids $r = 1$ and 2. The potentials satisfy the Laplace equation $\nabla^2 \phi_r = 0$ with interfacial kinematic boundary condition

$\left. \frac{\partial \eta}{\partial t} \right|_{y=\eta} = \left. \frac{\partial \phi_r}{\partial x} \frac{\partial \eta}{\partial x} \right|_{y=\eta} - \left. \frac{\partial \phi_r}{\partial y} \right|_{y=\eta}$, together with the Bernoulli equation $\rho_1 (\partial \phi_1 / \partial t - |\nabla \phi_1|^2 / 2) = \rho_2 (\partial \phi_2 / \partial t - |\nabla \phi_2|^2 / 2)$, where $\nabla = (\partial / \partial x, \partial / \partial y)$. The initial conditions are $\eta(x, 0) = a_0^+ \cos(kx)$ and $d\eta/dt|_{t=0} = a_0^+ \sigma \cos(kx)$, where $\sigma \equiv kA^+ \Delta u = v_0 / a_0^+$.

Substituting the perturbation expansions $\eta(x, t) = \sum_{n=1}^{\infty} \eta^{(n)}(x, t)$ and $\phi_r(x, y, t) = \sum_{n=0}^{\infty} \phi_r^{(n)}(x, y, t)$ into the equations, collecting terms of the same order and solving the ordinary differential equations in time yields $\eta^{(1)}(x, t) = a_0^+ (1 + \sigma t) \cos(kx)$, $\eta^{(2)}(x, t) = \frac{1}{2} k (\sigma a_0^+)^2 A^+ t^2 \cos(2kx)$ and $\eta^{(3)}(x, t) = -\frac{1}{24} k^2 (a_0^+)^3 \sigma \left\{ \left[4(A^+)^2 + 1 \right] \sigma^2 t^3 + 3\sigma t^2 + 6t \right\} \cos(kx) + \frac{1}{8} k^2 (a_0^+)^3 \sigma \left\{ \left[4(A^+)^2 - 1 \right] \sigma^2 t^3 - 3\sigma t^2 \right\} \cos(3kx)$ to third-order. The series approximation can be evaluated at the spike and bubble tip locations ($x = 0$ and at $x = \pi/k$, respectively) to yield the amplitude $a(t) = [\eta(0, t) - \eta(\pi/k, t)]/2$. This formulation gives an independent series for the spike and for the bubble, which can be used to evaluate separate bubble and spike amplitude models. The amplitude growth is given by

$$\frac{da}{dt} = \left\{ 1 - k^2 v_0 a_0^+ t + \left[(A^+)^2 - \frac{1}{2} \right] (k v_0 t)^2 \right\} v_0, \quad (16)$$

where v_0 is the Richtmyer velocity. Integrating gives

$$a(t) = a_0^+ + \left\{ 1 - \frac{k^2 v_0 a_0^+}{2} t + \frac{1}{3} \left[(A^+)^2 - \frac{1}{2} \right] (k v_0 t)^2 \right\} v_0 t. \quad (17)$$

Unfortunately, the range of validity of this finite Taylor series approximation is limited. Hence, Padé approximations (see the discussion of the Vandenboomgaerde *et al.* model below) are used to extend the approximation into the nonlinear regime:

$$\frac{da}{dt} = \frac{v_0}{1 + k^2 v_0 a_0^+ t + \max \left[0, (k a_0^+)^2 - (A^+)^2 + \frac{1}{2} \right] (k v_0 t)^2}. \quad (18)$$

Integrating Eq. (18) gives

$$a(t) = a_0^+ + \frac{2}{k \sqrt{4 \max \left[0, (k a_0^+)^2 - (A^+)^2 + \frac{1}{2} \right] - (k a_0^+)^2}} \times \tan^{-1} \left[\frac{k a_0^+ + 2 \max \left[0, (k a_0^+)^2 - (A^+)^2 + \frac{1}{2} \right] k v_0 t}{\sqrt{4 \max \left[0, (k a_0^+)^2 - (A^+)^2 + \frac{1}{2} \right] - (k a_0^+)^2}} \right]. \quad (19)$$

The choice of the Padé approximant P_2^0 for $(ka_0^+)^2 \geq (A^+)^2 - 1/2$ and P_1^0 for $(ka_0^+)^2 \leq (A^+)^2 - 1/2$ matches the experimental late-time growth. Note that v_0 in Eq. (18) can be replaced by $v_{lin}(t)$,⁴⁹ the numerically-determined linear growth rate obtained by solving the full set of compressible perturbation equations.¹ In this case, Eq. (18) must be integrated numerically to obtain $a(t)$. The Zhang-Sohn model does not predict the generally accepted $1/t$ growth at late times.

2. The Vandenboomgaerde-Gauthier-Mügler model

Vandenboomgaerde, Gauthier and Mügler⁵⁰ proposed a simplified version of the Zhang-Sohn perturbation expansion. First, choose $\sigma \equiv \frac{k\Delta u}{2} \left(A^+ + \frac{A^-}{1-\Delta u/u_{\text{shock}}} \right)$ such that $a_0^- \sigma$ gives the right side of Eq. (12), where u_{shock} is the shock velocity. Noting that an accurate perturbation series can be obtained by retaining only the secular terms (i.e., the terms with the largest unbounded part), only the largest power from each term of the Zhang-Sohn solution is retained to third-order: $\eta^{(1)}(x, t) = a_0^+ (1 + \sigma t) \cos(kx)$, $\eta^{(2)}(x, t) = \frac{1}{2} (a_0^+ \sigma t)^2 k A^+ \cos(2kx)$ and $\eta^{(3)}(x, t) = -\frac{1}{8} (ka_0^+)^2 (\sigma t)^3 \left\{ \frac{1}{3} [4(A^+)^2 + 1] \cos(kx) - [4(A^+)^2 - 1] \cos(3kx) \right\}$. Such an approximation is usually valid for large times, and the first two terms of this series are identical to the Zhang-Sohn series, so that very good agreement is expected between the predictions of this model and the Zhang-Sohn model at small times. An advantage of this perturbation method is that higher order terms can be easily computed.

As only the high-order terms in the series are retained, the determination of the coefficients shifts from integrating in time to solving an algebraic system. The growth rate is given by the $2N$ th-degree polynomial

$$\frac{da}{dt} = a_0^+ \sigma \sum_{n=0}^N (2n+1) (k a_0^+ \sigma t)^{2n} P_{2n+1}(A^+), \quad (20)$$

where P_{2n+1} are the series approximation in A^+ (not shown). Integrating gives

$$a(t) = a_0^+ + \frac{1}{k} \sum_{n=0}^N (k a_0^+ \sigma t)^{2n+1} P_{2n+1}(A^+), \quad (21)$$

where $N = 4$ and 5 correspond to the ninth- and eleventh-degree cases, respectively. The P_6^4 Padé approximant to da/dt is

$$\frac{da}{dt} = \frac{\sum_{p=0}^4 A_p (k a_0^+ \sigma t)^p}{\sum_{q=0}^6 B_q (k a_0^+ \sigma t)^q}, \quad (22)$$

where the Padé coefficients $\{A_p\}$ and $\{B_q\}$ are not given here.

3. The Matsuoka-Nishihara-Fukuda model

Matsuoka, Nishihara and Fukuda⁵¹ proposed a new formulation of the Zhang-Sohn kinematic boundary condition to account for interface stretching: this boundary condition was replaced by $\bar{\mathbf{u}} \cdot \mathbf{n} = [(\rho_1 \nabla \phi_1 + \rho_2 \nabla \phi_2) \cdot \mathbf{n}] / (\rho_1 + \rho_2)$ and $\bar{\mathbf{u}} \cdot \mathbf{s} = [(\rho_1 \nabla \phi_1 + \rho_2 \nabla \phi_2) \cdot \mathbf{s}] / (\rho_1 + \rho_2)$ evaluated on the interface, where $\bar{\mathbf{u}} \equiv (\rho_1 \mathbf{u}_1 + \rho_2 \mathbf{u}_2) / (\rho_1 + \rho_2)$ is the density-weighted mean velocity, \mathbf{n} is the unit normal vector to the interface, and \mathbf{s} is the unit tangent vector to the interface. The perturbation expansion yields different expansions for the bubble and spike amplitude. When the first three terms are considered, the bubble and spike velocities are given by

$$\begin{aligned} \frac{\partial a_{b,s}}{\partial \tau} = & \left[\mp (A^+)^2 \pm \frac{1}{2} \right] \tau^2 \\ & + \left[\mp 2 (A^+)^2 k a_0^+ + A^+ \pm k a_0^+ \right] \tau \\ & + \left[\mp 2 (A^+)^2 \pm \frac{3}{2} \right] (k a_0^+)^2 + \frac{k a_0^+ A^+}{2} \mp 1, \end{aligned} \quad (23)$$

where τ is the rescaled time [Eq. (5)] and the upper (+ or -) and lower (- or +) sign in \pm or \mp denotes the bubble and spike, respectively. The asymptotic series can be improved by considering P_2^0 Padé approximants:

$$\frac{\partial a_{b,s}}{\partial \tau} = \frac{f_{\pm}^3}{\left\{ f_{\pm} \left[(A^+)^2 - \frac{1}{2} \right] + g_{\pm}^2 \right\} \tau^2 - f_{\pm} g_{\pm} \tau + f_{\pm}^2}, \quad (24)$$

where $f_{\pm} \equiv \mp \left[2 (A^+)^2 - 3/2 \right] (k a_0^+)^2 + A^+ k a_0^+ / 2 \mp 1$ and $g_{\pm} \equiv \mp 2 (A^+)^2 k a_0^+ + A^+ \pm k a_0^+$.

Integrating gives

$$\begin{aligned} a_{b,s}(\tau) = & a_{b,s}(0) + \frac{f_{\pm}^2}{\sqrt{f_{\pm} \left[(A^+)^2 - \frac{1}{2} \right] + g_{\pm}^2}} \\ & \times \tan^{-1} \left\{ \frac{2 \left\{ f_{\pm} \left[(A^+)^2 - \frac{1}{2} \right] + g_{\pm}^2 \right\} \tau - f_{\pm} g_{\pm}}{\sqrt{f_{\pm} \left[(A^+)^2 - \frac{1}{2} \right] + g_{\pm}^2}} \right\}. \end{aligned} \quad (25)$$

4. The Sadot et al. model

The empirical Sadot *et al.*⁵² model for the Richtmyer-Meshkov instability is based on fits to experimental data and on asymptotic growth laws. This model was extensively tested

against experimental data and appears to be valid over $Ma = 1.3\text{--}3.5$ in air and SF_6 . The model provides a single formula that captures the initial linear growth, and the later nonlinear growth of the bubble and spike,

$$\frac{da_{b,s}}{dt} = \frac{(1 + k v_0 t) v_0}{1 + (1 \pm A^+) k v_0 t + \frac{1 \pm A^+}{1 + A^+} \frac{(k v_0 t)^2}{2\pi C}} \quad (26)$$

[the upper (+) and lower (−) sign in \pm denotes the bubble and spike, respectively] where $C = 1/(3\pi)$ for $A^+ \geq 0.5$. In the limit $A^+ \rightarrow 0$, $C = 1/(2\pi)$. Integrating Eq. (26) gives

$$a_{b,s}(t) = a_{b,s}(0) + \frac{2 - 2\pi C (1 + A^+)}{k \sqrt{\frac{2}{\pi C} \frac{1 \pm A^+}{1 + A^+} - (1 \pm A^+)^2}} \tan^{-1} \left[\frac{1 \pm A^+ + \frac{1 \pm A^+}{1 + A^+} \frac{k v_0 t}{\pi C}}{\sqrt{\frac{2}{\pi C} \frac{1 \pm A^+}{1 + A^+} - (1 \pm A^+)^2}} \right] + \frac{\pi C}{k} \frac{1 + A^+}{1 \pm A^+} \ln \left[1 + (1 \pm A^+) k v_0 t + \frac{1 \pm A^+}{1 + A^+} \frac{(k v_0 t)^2}{2\pi C} \right]. \quad (27)$$

This model is consistent with $1/t$ asymptotic growth at late times.

C. Potential flow models

Potential flow models describe the amplitude evolution of the instability through the late-time, nonlinear regime by the bubble and spike velocity evolution. Layzer⁵³ developed the first potential flow model to describe the Rayleigh-Taylor instability, which was subsequently extended to the Richtmyer-Meshkov instability by others. These models predict that the bubble velocity in a Richtmyer-Meshkov instability approaches zero asymptotically.

1. The Goncharov model

Goncharov⁵⁴ extended the two-dimensional Layzer model to the $A^+ \neq 1$ case using a parabolic expansion $\eta(t) = h(t) + \xi(t)x^2$ near the bubble and spike tips and initial perturbations $\phi_1(x, y, t) = a_1(t) \cos(kx) e^{k[y-h(t)]}$ and $\phi_2(x, y, t) = b_1(t) \cos(kx) e^{-k[y-h(t)]} + b_2(t)y$. This ansatz requires the solution of five ordinary differential equations for the functions $a_1(t)$, $b_1(t)$, $b_2(t)$, $h(t)$ and $\xi(t)$. The asymptotic bubble velocity for the Richtmyer-Meshkov instability is obtained by taking the $t \rightarrow \infty$ limit of the result:

$$v_b(t) = \frac{3 + A^+}{3(1 + A^+) k t}. \quad (28)$$

2. The Sohn models

Sohn⁵⁵ also extended the Layzer model to fluids with arbitrary density ratios. The approach differs from that of Goncharov in the use of a simpler form for the initial potentials, $\phi_1(x, y, t) = -a(t) \cos(kx) e^{ky}$ and $\phi_2(x, y, t) = a(t) \cos(kx) e^{-ky}$, leading to a simplified system requiring the solution of three ordinary differential equations for the functions $a(t)$, $h(t)$ and $\xi(t)$. The Richtmyer-Meshkov asymptotic bubble velocity is given by

$$v_b(t) = \frac{2}{(2 + A^+) k t}. \quad (29)$$

The ratio of Eq. (28) and Eq. (29), $(3 + A^+)(2 + A^+)/[6(1 + A^+)]$ quantifies the difference between the Sohn and Goncharov models. In the present case with $A^+ = 0.6274$ (see Table II) the ratio indicates that the predictions are within 3% of one another.

Sohn⁵⁶ also extended the Zufiria model^{57,58} to arbitrary Atwood numbers. In the Zufiria model, originally developed to model bubbles of different size, the velocity potential is obtained by approximating the bubble as a point source. The bubble velocity is

$$v_b(t) = \left[\frac{3 + A^+}{3(1 + A^+)} - \frac{1}{q} + \frac{2A^+}{3(1 + A^+)q^2} \right] \frac{1}{k t}, \quad (30)$$

where $q = q(A^+)$ is the root of the cubic polynomial $(3 - A^+)q^3 - (21 + 9A^+)q^2 + (3 + 15A^+)q - 4A^+ = 0$. Comparing the Zufiria model [Eq. (30)] with the Goncharov model [Eq. (28)] shows that the Zufiria model contains two additional terms, resulting in a predicted asymptotic velocity $\approx 14\%$ smaller for the present value $A^+ = 0.6274$.

3. The Mikaelian model for the bubble amplitude

Mikaelian⁵⁹ obtained an analytic expression for the transition of the bubble amplitude from the linear to the nonlinear regime by combining the Richtmyer initial growth [Eq. (6)] with the Goncharov late-time bubble growth for arbitrary Atwood numbers [Eq. (28)]. Mikaelian used a technique attributed by Layzer⁵³ to Fermi for combining the initial and asymptotic bubble velocities. However, unlike the Fermi model, in which the transition between the linear and asymptotic velocity occurs when the two velocities are equal, Mikaelian proposed a transition between these velocities at an earlier time corresponding to $a_b = 1/(3k)$, resulting in decreasing the bubble amplitude in accord with numerical and

experimental observations. For times $t < t^* \equiv [1/(3ka_0^+) - 1]/(kA^+\Delta u)$, the amplitude is given by Eq. (6), so that $a_b(t^*) = 1/(3k)$. The bubble amplitude is given by

$$a_b(t) = \frac{1}{3k} \left\{ 1 + \frac{3 + A^+}{1 + A^+} \ln \left[1 + \frac{3k v_0 (1 + A^+)}{3 + A^+} (t - t^*) \right] \right\} \quad (31)$$

for times $t > t^*$, so that v_b agrees with Eq. (28) in the limit of large times.

IV. COMPARISON OF SIMULATION AMPLITUDES TO EXPERIMENTAL DATA AND TO MODEL PREDICTIONS

In this section, the perturbation amplitude growth obtained from the fifth- and ninth-order simulations is compared to the experimental data of Collins and Jacobs¹⁵ and to the predictions of the models in Sec. III. First, the method used to determine the amplitudes from the simulations is presented. Next, these amplitudes are compared to the experimental data points. The ninth-order amplitude is then compared to the predictions of impulsive and nonlinear perturbation models, with the model parameters computed self-consistently from the simulation. The bubble and spike amplitudes are also compared with the predictions of bubble and spike amplitude growth models and with the asymptotic bubble velocities predicted by potential flow models. A local and a global metric is used to quantify the differences between the various predictions and the simulation and experimental data—an average fractional deviation and the ratio of the model predictions to the ninth-order amplitude, respectively. Prior to differentiating a , the numerical amplitude was smoothed using a standard five-point moving average⁶⁰ to smooth oscillations otherwise present.

A. Determination of the bubble, spike and mixing layer amplitudes

Consider the mole fraction

$$X(x, y, t) = \frac{m(x, y, t) M_1}{[1 - m(x, y, t)] M_2 + m(x, y, t) M_1}, \quad (32)$$

where M_1 and M_2 are the molecular weights of the air(acetone) and SF₆, respectively, and m is the mass fraction of SF₆. Spatially-averaging $X(x, y, t)$ in the spanwise direction gives

$$\bar{X}(x, t) = \frac{1}{L_y} \int_0^{L_y} X(x, y, t) dy, \quad (33)$$

where L_y is the spanwise domain width. The bubble and spike tip locations, $\ell_b(t)$ and $\ell_s(t)$, are then defined as the x position where $\bar{X} \leq 1 - \epsilon$ and $\bar{X} \geq \epsilon$, respectively, with $\epsilon = 0.01$ in the present investigation.⁶¹ The width is given by $h(t) = \ell_b(t) - \ell_s(t)$. This measure of the width was chosen, rather than using the distance between the lines $x = \lambda/2$ and $x = \lambda$, in order to also examine the evolution of the width following reshock when the interface becomes multi-valued and disordered. To obtain the bubble and spike amplitudes separately, *a simulation without an initial perturbation, but otherwise identical to the Richtmyer-Meshkov instability simulation, was performed to obtain the interface position ℓ_{int}* , so that the bubble and spike amplitudes are determined separately by $a_b(t) \equiv \ell_b(t) - \ell_{\text{int}}(t)$ and $a_s(t) \equiv \ell_{\text{int}}(t) - \ell_s(t)$, respectively.

The interface and shock locations from the ninth-order simulation are exhibited in the x - t diagram of Fig. 5. The interface location $\ell_{\text{int}}(t)$ is shown as a solid line. The bubble and spike tip locations are indicated by the dash-dot and dashed lines, respectively. The horizontal distance between the spike and bubble tips represents the width $h(t)$ (see Fig. 4 for a schematic of the amplitudes). The shock reflects from the end wall at ≈ 4 ms and reshock occurs at $t \approx 6.4$ ms when the shock wave refracts at the evolving interface, generating a transmitted shock in the air(acetone) and a reflected rarefaction in the SF₆ (the reflected rarefaction is not shown in the x - t diagram). The transmitted shock following reshock moves faster than the incident shock, as indicated by the change in slope, corresponding to a slow-fast refraction.⁶² Following reshock, the interface is compressed (as seen from the kink in the bubble and spike locations) and moves away from the end wall of the test section. Additionally, the amplitude grows more rapidly than prior to reshock: the increased growth is due to the additional vorticity deposited on the evolving interface during reshock (see Part II). The reshock (inversion) process occurs over a time interval of ≈ 0.2 – 0.3 ms.

The following conventions are used when comparing the numerical simulation data to the predictions of the models presented in Sec. III. The amplitude growth rate is adjusted to account for the diffuse interface by including the growth reduction factor ψ by

$$\frac{da}{dt} \longrightarrow \frac{1}{\psi} \frac{da}{dt}, \quad (34)$$

which was also used by Collins and Jacobs¹⁵ to compare their amplitude data to growth model predictions. The time and initial velocity are also rescaled according to (5), where a_0^+ is determined by multiplying the pre-shock amplitude a_0^- by the compression factor

$\eta_{\text{comp}} = 1 - \Delta u/u_{\text{shock}}$. Reshock occurs at $\tau \lesssim 5$ ms. In general, when a model predicts the growth rate, da/dt , the amplitude a can be obtained by solving an initial value problem using a fourth-order Runge-Kutta scheme (for example).

Table II gives the parameters used in the amplitude growth model predictions, which are also compared to the experimental values (see Table 1 in Ref. 15). An 11% discrepancy exists between the interface velocity Δu after the passage of the incident shock reported here and the experimental value [the experimental value of Δu can be inferred from Eq. (6), which was also used by Collins and Jacobs]. A one-dimensional analysis assuming ideal gas behavior and a non-ventilated shock tube gives $\Delta u = 6420$ cm/s while the measured speed is only $\Delta u = 6060$ cm/s, which is attributed to the slots in the shock tube.¹⁵ The single-gamma limitation of the present simulations only accounts for the difference between the speed of 6731 cm/s and the one-dimensional shock refraction theory value of 6420 cm/s.

B. Comparison to experimental amplitude data

The fifth- and ninth-order simulation amplitudes are compared to the Collins and Jacobs¹⁵ experimental amplitude data in Fig. 6. The layer begins growing immediately following the initial shock passage. The initial rapid growth saturates at ≈ 4 ms, and reshock occurs ≈ 2.4 ms later. During reshock, the amplitude is compressed by ≈ 1 cm and subsequently grows rapidly. Comparison of the numerical and experimental data indicates very good agreement up to the time at which the driver-based expansion present in the experiment (but not present in either the simulations or models) begins to expand the layer at ≈ 4.5 –5 ms (see Fig. 4 of Collins and Jacobs¹⁵). The subsequent discrepancy is due to the arrival of the driver-based expansion wave not modeled in the simulation and to the difference in interface velocity between the simulation and experiment. The driver-based expansion decelerates the interface and, thus, delays the reshock to $t > 8$ ms in the experiment. For $t > 3$ ms, the fifth-order amplitude is slightly larger than the ninth-order amplitude up to reshock. The instability evolution in the experiment is essentially two-dimensional prior to reshock (by virtue of the manner in which the initial perturbation was produced), and becomes three-dimensional following reshock, as the shock-interface interaction excites fluctuations in all spatial directions. Thus, it is reasonable to expect that a two-dimensional numerical simulation can reproduce the experimentally-measured amplitude growth prior to

reshock. However, three-dimensional simulations are necessary to more accurately estimate the mixing layer width evolution and other quantities following reshock.

The simulation bubble and spike amplitudes are also shown in Fig. 6: the amplitude asymmetry is due to the relatively large Atwood number. Prior to reshock, the fifth-order bubble and spike amplitudes are slightly larger than the ninth-order amplitudes. Following reshock, the fifth-order bubble amplitude is slightly larger than the ninth-order amplitude, but the converse is true for the spike amplitude. To globally quantify the difference between the experiment and simulation, the *average fractional deviation*⁴¹

$$\Delta = \frac{1}{N} \sum_{i=1}^N \frac{|a_{\text{sim}}(t_i) - a_{\text{exp}}(t_i)|}{a_{\text{sim}}(t_i)} \quad (35)$$

between the simulation data, $a_{\text{sim}}(t_i)$, and the experimental data points, $a_{\text{exp}}(t_i)$, is computed at the times t_i ($i = 1, 2, \dots, N$), where $N = 51$ is the number of experimental data points and the simulation amplitudes are spline interpolated to the experimental times t_i . The results $\Delta_{\text{fifth}} = 0.1$ and $\Delta_{\text{ninth}} = 0.11$ indicate that both amplitude predictions are very similar. As a result, only the ninth-order amplitude is considered in the next sections.

C. Comparison to the predictions of impulsive models

Here, simulation and experimental data are compared to the predictions of the impulsive models described in Sec. III A when they are corrected for the case of a diffuse interface by (34). The ninth-order amplitude is compared to the prediction of the Richtmyer¹ model [Eq. (6)], the Meyer and Blewett⁴³ model [Eq. (8)], the Fraley⁴⁴ model [Eq. (10)] and the Vandenboomgaerde et. al.⁴⁶ model [Eq. (12)] in Fig. 7. The normalized amplitude $k[a(\tau) - a_0]$ is shown versus the normalized time τ given by Eq. (5). The impulsive models all correctly capture the initial growth for $\tau < 1$, although they slightly overestimate the amplitude. For $\tau > 1$ (typically referred to as the *nonlinear growth phase*), nonlinear effects ensue and the models significantly overestimate the amplitude and its growth rate. The impulsive models predict a constant growth rate, whereas the simulation growth decreases steadily in time as in the experiment due to nonlinear saturation effects. Thus, it is difficult to determine which model agrees best with the data at early times. However, this is not the case for all initial conditions, as plotting the normalized growth rate as a function of the shock strength and comparing the predictions of the impulsive models to the Fraley (exact)

solution would show.⁴⁵ For strong shocks the impulsive models exhibit large deviations from the Fraley solution, indicating that they are no longer valid.

D. Comparison to the predictions of perturbation models

The numerical and experimental amplitude data are compared here to the predictions of the nonlinear perturbation models summarized in Sec. III B when they are corrected for the case of a diffuse interface by (34). The experimental and simulation data are compared to the perturbation series solutions of Zhang and Sohn⁴⁹ [Eq. (16)], Vandenboomgaerde *et al.*⁵⁰ [Eq. (20)] of degree 9 and 11, and Matsuoka *et al.*⁵¹ [Eq. (23)] in Fig. 8. Also shown in Fig. 8 is a comparison of the normalized growth rate, $kda/d\tau$, from the ninth-order simulation to the predictions of the nonlinear perturbation series models versus the normalized time τ : the perturbation series capture the initial growth, but quickly diverge. In particular, the eleventh-order Vandenboomgaerde *et al.* perturbation series has a smaller radius of convergence than the ninth-order series: the series can be extended via Padé approximants to expand the radius of convergence.

The experimental and numerical data are compared to the predictions of the nonlinear models extended via Padé approximants in Fig. 9. Shown are the Zhang-Sohn P_2^0 Padé approximant [Eq. (18)], the Vandenboomgaerde *et al.* P_6^4 Padé approximant [Eq. (22)] and the Matsuoka *et al.* P_2^0 Padé approximant [Eq. (24)]. The prediction of the Sadot *et al.*⁵² empirical model [Eq. (26)] is also shown. The Zhang-Sohn and Vandenboomgaerde *et al.* Padé model predictions agree well with the experimental data in the linear and nonlinear regimes. The Vandenboomgaerde *et al.* Padé approximant captures the correct behavior at early times $\tau < 1$, but overestimates the amplitude at later times. The Zhang-Sohn Padé approximant underestimates the amplitude for $\tau < 1$, but gives the correct behavior for later times. The Matsuoka *et al.* Padé approximant correctly predicts the amplitude at early times but underestimates the amplitude at late times. Also shown in Fig. 9 is the normalized growth rate, $kda/d\tau$, from the ninth-order simulation and the predictions of the nonlinear models. The nonlinear models considered here generally capture both the initial and late-time amplitude growth.

To determine which of the models gives the amplitude growth in best agreement with the simulation data, the ratios of the Zhang-Sohn (Padé), Vandenboomgaerde *et al.*

al. (Padé), Matsuoka *et al.* (Padé) and Sadot *et al.* models, to the simulation data, $[a_{\text{mod}}(\tau) - a_0]/[a_{\text{sim}}(\tau) - a_0]$, are presented in Fig. 10. For $\tau \gtrsim 0.4$, the Zhang-Sohn Padé model is in best agreement with the simulation, overestimating the data by $< 5\%$ over the evolution time. Collins and Jacobs¹⁵ reported that their data is in best agreement with the amplitude predicted by the Sadot *et al.* model. Only the Sadot *et al.* model has the correct growth at late time, whereas the amplitudes from the other models attain a maximum between $\tau \approx 0.7\text{--}1.6$ and then rapidly decay up to reshock $\tau \lesssim 5$. To further support the conclusions of the present investigation, the average fractional deviation [Eq. (35)] is also computed between the simulation results and the model predictions, Δ_{sim} in Table III. The agreement between the simulation amplitudes and the experimental data, but the different conclusions regarding which amplitude growth model best agrees with the simulation and experimental data, motivates a study of the sensitivity of the model predictions to the model input parameters v_0 , A^+ , a_0^+ and Δu presented in Sec. IVF

E. Comparison of bubble and spike amplitudes and velocities to the predictions of potential and perturbation models

A comparison of the bubble and spike amplitudes from the ninth-order simulation to the Matsuoka *et al.* [Eq. (24)] and the Sadot *et al.* [Eq. (26)] model predictions, when they are corrected for the case of a diffuse interface by (34), is shown in Fig. 11. The bubble amplitude prediction of the Mikaelian model [Eq. (31)] is also shown. The Matsuoka *et al.* model overestimates the bubble and spike amplitude. The Sadot *et al.* and Mikaelian models predict very good agreement for the bubble amplitude from the linear through the nonlinear regime. However, the Sadot *et al.* model overestimates the spike amplitude from the simulation. The ratio of the predicted bubble and spike amplitudes to the simulation results, respectively, is also shown in Fig. 11. The ratio shows an initial difference between the predictions of the Mikaelian and Sadot *et al.* models for the bubble amplitudes. However, this difference decreases, and by 3 ms the predictions of both models are nearly identical. For short times following the passage of the shock, the spike amplitude from the Matsuoka *et al.* model is in close agreement with the simulation amplitude. See Table III for the average fractional deviation [Eq. (35)] computed between the simulation results and the model predictions.

A comparison between the bubble and spike velocities from the simulation with the asymptotic bubble velocities predicted by the Goncharov model [Eq. (28)], the Sohn-Layzer model [Eq. (29)] and the Sohn-Zufiria model [Eq. (30)], and the predictions for the bubble and spike velocities from the Matsuoka *et al.*, Sadot *et al.* and Mikaelian models, are shown in Fig. 12. The asymptotic bubble velocities predicted by potential theory and the Sadot *et al.* and Mikaelian models are in very good agreement. The Sohn-Layzer and Goncharov models give nearly identical predictions. The bubble velocities predicted by the Sadot *et al.* model, the Mikaelian model, and the asymptotic velocity predicted by the Sohn-Zufiria model are all in very close agreement and are closest to the simulation bubble velocity. The Matsuoka *et al.* model underpredicts the late-time bubble velocity. The Sadot *et al.* and Matsuoka *et al.* model overpredicts and underpredicts the spike velocity, respectively.

F. Comparison of amplitude model predictions using experimental and numerical model parameters

The very good agreement between the numerical simulations and experiment shown in the previous section does not extend to the predictions of nonlinear amplitude growth models. When the amplitude model parameters, v_0 , A^+ , a_0^+ and Δu , are computed using the experimental data, the Sadot *et al.* model gives the best agreement with the experimental and simulation data; by contrast, when the parameters are computed using the simulation data, the Zhang-Sohn Padé model gives the best agreement. This is primarily due to the different initial growth velocity v_0 in the simulations and the experiment, and to the differences in A^+ , a_0^+ and Δu . These observations and the single-gamma approximation used in the present simulations motivate a comparison of the nonlinear amplitude growth model predictions when the model parameters are computed using the experimental data (see Table II and Table 1 in Ref. 15) to those when the parameters are computed using the simulation data.

A comparison of the Zhang-Sohn Padé, Vandenboomgaerde *et al.* Padé, Matsuoka *et al.* Padé and Sadot *et al.* model predictions computed using experimental and simulation values for v_0 , A^+ , a_0^+ and Δu is presented in Fig. 13. The Zhang-Sohn and the Sadot *et al.* models are the most sensitive to changes in these model parameters. The predicted amplitudes obtained using the simulation parameters are in general larger than those obtained using

the experimental parameters, due to the difference in the initial velocity of the interface: specifically, v_0 from the simulation is larger than the corresponding experimental value. By contrast, the Vandenboomgaerde *et al.* model does not exhibit significant sensitivity to the variation of the experimental or simulation model parameters. When the experimental parameters are used, the Vandenboomgaerde *et al.* model prediction is in best agreement with the simulation data; however, when the simulation parameters are used, the Zhang-Sohn model prediction is in best agreement with the simulation amplitude. The normalized amplitude growth rates predicted by the nonlinear growth models and the ratios of the model predictions to the ninth-order simulation data are also presented in Fig. 13.

A similar parametric sensitivity study is presented in Fig. 14 for the bubble and spike amplitudes and velocities, and their ratios to the corresponding simulation quantities. In general, when the experimental parameters are used, the predicted bubble and spike amplitudes are lower than those computed using the simulation parameters, resulting in better agreement with the simulation results. The velocities do not show a similar difference: in the case of the bubble velocity, the predictions obtained using the simulation and experimental parameters are in very close agreement.

The differences between the predictions of the models when the parameters are computed using the experimental and simulation data is further quantified using the average fractional deviation [Eq. (35)] between the simulation amplitude data $a_{\text{sim}}(t)$ and the model predictions $a_{\text{mod}}(t)$, Δ_{exp} and Δ_{sim} , respectively (see Table III). The Vandenboomgaerde *et al.* model prediction using the experimental parameters is in best agreement with the simulation amplitude, while the Zhang-Sohn Padé model prediction using the simulation parameters is in best agreement with the simulation amplitude. The Mikaelian bubble amplitude model prediction using the experimental parameters is in best agreement with the simulation bubble amplitude, while the Sadot *et al.* model prediction using the simulation parameters is in best agreement with the simulation bubble amplitude. The Sadot *et al.* spike amplitude model prediction using the experimental parameters is in best agreement with the simulation spike amplitude, while the Matsuoka *et al.* Padé model prediction using the simulation parameters is in best agreement with the simulation spike amplitude. Table III also shows the average fractional deviation between the experimental amplitude data $a_{\text{exp}}(t)$ and the model predictions $a_{\text{mod}}(t)$ when the model predictions are computed using the experimental and simulation parameters, Δ_{exp}^e and Δ_{sim}^e , respectively: the Matsuoka *et*

al. Padé model prediction using the experimental parameters is in best agreement with the experimental amplitude, while the Zhang-Sohn Padé model prediction using the simulation parameters is in best agreement with the simulation amplitude.

V. DISCUSSION AND CONCLUSIONS

The high-resolution fifth- and ninth-order weighted essentially non-oscillatory (WENO) shock-capturing method was applied to the classical two-dimensional, reshocked single-mode Richtmyer-Meshkov instability with a uniform grid resolution corresponding to 256 points per initial perturbation wave length. The initial conditions and computational domain approximated the Mach 1.21 air(acetone)/SF₆ shock tube experiment of Collins and Jacobs.¹⁵ Only the test section of the shock tube was simulated, so that the driver-based expansion and reflected rarefaction waves present in the experiment were not captured in the simulations. This is a convenient idealization, as the amplitude growth models considered do not account for these waves. A single value of the adiabatic exponent was used. Molecular dissipation and diffusion terms in the governing equations were neglected.

The simulation density and the experimental PLIF images from the $Ma = 1.21$ Collins and Jacobs experiment were in very good qualitative agreement up to the time at which the driver-based expansion affects the experimental amplitude growth (and before reshock when three-dimensional effects are unimportant). The comparison of densities from the fifth- and ninth-order simulations demonstrates that higher-order reconstruction better captures secondary instabilities, the roll-ups are tighter and sharper, and more fine-scale structures are present as a result of decreased numerical dissipation and diffusion. Following reshock, the experiment and simulations show distinctively different flow structures due to the absence of the driver-based expansion, the difference in the interface velocities, and the increased importance of three-dimensional effects that are not captured in the simulations. As a result, the simulation densities are qualitatively similar to the corrected experimental density PLIF images, but lag in time by ≈ 1 ms.

Very good quantitative agreement was found between the fifth- and ninth-order amplitude and the experimental data points up to the time at which the driver-based expansion in the experiment (but not present in either the simulations or models) begins to expand the layer prior to reshock. A comprehensive comparison of a large number of widely used

models applied to the present simulations and to the experimental data with the diffuse interface correction (34) was performed. The ninth-order simulation data was compared to the predictions of the: (1) linear impulsive models of Richtmyer,¹ Meyer and Blewett,⁴³ Fraley⁴⁴ and Vandenboomgaerde *et al.*⁴⁶; (2) weakly-nonlinear perturbation models of Zhang and Sohn,⁴⁹ Vandenboomgaerde *et al.*⁵⁰ and Matsuoka *et al.*,⁵¹ and; (3) nonlinear empirical model of Sadot *et al.*⁵² The bubble and spike velocities were also compared to the predictions of the potential models of Goncharov⁵⁴ and Sohn.^{55,56} In addition, the bubble amplitude was compared to the prediction of the Mikaelian⁵⁹ model. A local and a global metric was used to quantify the differences between the amplitude growth model predictions and the simulation and experimental data—the ratio of the model predictions to the ninth-order amplitude as a function of time (local) and the average fractional deviation (global). As expected, very good agreement with the linear models was found at early times. At later times, the simulation data was shown to be in very good agreement with the predictions of the Zhang-Sohn Padé amplitude growth model before reshock. Thus, this component of the present work provides a partial validation of the WENO method against pre-reshock single-mode Richtmyer-Meshkov instability experimental data.

Motivated by the agreement between the simulation amplitudes and the experimental data, but the different conclusions regarding which amplitude growth model best agrees with the simulation and experimental data, the sensitivity of the model predictions to changes in the model parameters v_0 , A^+ , a_0^+ and Δu was also investigated. First, the parameters from the Collins-Jacobs experiment and from the present simulation were compared. Then it was shown that the predictions of the nonlinear amplitude growth models are quite sensitive to variations in these parameters. In particular, when experimental parameters are used, the prediction of the Sadot *et al.* model is in best agreement with the experimental and simulation amplitude; by contrast, when the simulation parameters are used, the prediction of the Zhang-Sohn Padé model is in best agreement with the experimental and simulation amplitude. *These results indicate that caution should be used when applying nonlinear amplitude growth models to experiments and to numerical simulations and interpreting their predictions. Moreover, it may not be possible to distinguish between the predictions of different models when the parameters are varied within the experimentally reported error bars.*

While the present simulations are idealized in that they consider only the shock tube test section, two-dimensional flow and a single gamma, the agreement with experimental

data prior to reshock provides encouragement for the continued quantitative investigation of shock-induced complex hydrodynamic flows and mixing using high-order WENO methods. Other researchers have also advocated the WENO method for simulating compressible flows.^{63–67} The hybridization of WENO reconstructions with high-order central-difference or spectral schemes⁶⁸ to improve computational efficiency and reduce numerical dissipation in regions away from discontinuities is currently under development and will be used in future investigations of the physics of Richtmyer-Meshkov mixing.

Acknowledgments

The authors thank Dr. Jeffrey W. Jacobs for clarifying aspects of the experiment considered in this work, Dr. Vitaly V. Krivets for providing details not originally presented in the description of the experiments, and Dr. Karnig O. Mikaelian for useful comments on the perturbation amplitude models. Marco Latini gratefully acknowledges support from the Air Force Office of Scientific Research through the National Defense Science and Engineering Graduate Fellowship and the Caltech Accelerated Strategic Computing (ASC) Center. Wai Sun Don gratefully acknowledge the support of this work by the DOE under contract number DE-FG02-98ER25346 and the AFOSR under contract number FA9550-05-1-0123. This work was also performed under the auspices of the U.S. Department of Energy by the University of California, Lawrence Livermore National Laboratory under contract No. W-7405-Eng-48.

-
- ¹ R. D. Richtmyer, “Taylor instability in shock acceleration of compressible fluids,” *Comm. Pure Appl. Math.* **8**, 297 (1960).
 - ² E. E. Meshkov, “Instability of the interface of two gases accelerated by a shock wave,” *Sov. Fluid Dyn.* **4**, 101 (1969).
 - ³ N. J. Zabusky, “Vortex paradigm for accelerated inhomogeneous flows: Visiometrics for the Rayleigh-Taylor and Richtmyer-Meshkov environments,” *Ann. Rev. Fluid Mech.* **31**, 495 (1999).
 - ⁴ M. Brouillette, “The Richtmyer-Meshkov instability,” *Ann. Rev. Fluid Mech.* **34**, 445 (2002).
 - ⁵ J. D. Lindl, “Development of the indirect-drive approach to inertial confinement fusion and the target physics basis for ignition and gain,” *Phys. Plasmas* **2**, 3933 (1995).

- ⁶ S. Nakai and H. Takabe, “Principles of inertial confinement fusion—physics of implosion and the concept of inertial fusion energy,” *Rep. Prog. Phys.* **59**, 1071 (1996).
- ⁷ J. D. Lindl, *Inertial Confinement Fusion: The Quest for Ignition and Energy Gain Using Indirect Drive* (AIP Press, New York, 1998).
- ⁸ S. Atzeni and J. Meyer-ter Vehn, *The Physics of Inertial Confinement Fusion: Beam Plasma Interaction, Hydrodynamics, Hot Dense Matter*, vol. 125 of *International Series of Monographs on Physics* (Oxford University Press, New York, 2004).
- ⁹ G. J. Hendricks, *Two Mechanisms of Vorticity Generation in Combusting Flow Fields*, Ph.D. thesis, California Institute of Technology (1986).
- ¹⁰ S. W. Falk and W. D. Arnett, “A theoretical model for type II supernovae,” *Astrophys. J.* **180**, L65 (1973).
- ¹¹ W. D. Arnett, “Supernova theory and supernova 1987A,” *Astrophys. J.* **319**, 136 (1987).
- ¹² W. D. Arnett, B. A. Fryxell, and E. Müller, “Instabilities and nonradial motion in SN-1987A,” *Astrophys. J.* **341**, L63 (1989).
- ¹³ J. Kane, R. P. Drake, and B. A. Remington, “An evaluation of the Richtmyer-Meshkov instability in supernova remnant formation,” *Astrophys. J.* **511**, 335 (1999).
- ¹⁴ D. Arnett, “The role of mixing in astrophysics,” *Astrophys. J. Suppl.* **127**, 213 (2000).
- ¹⁵ B. D. Collins and J. W. Jacobs, “PLIF flow visualization and measurements of the Richtmyer-Meshkov instability of an air/SF₆ interface,” *J. Fluid Mech.* **464**, 113 (2002).
- ¹⁶ G. Peng, N. J. Zabusky, and S. Zhang, “Vortex-accelerated secondary baroclinic vorticity deposition and late-intermediate time dynamics of a two-dimensional Richtmyer-Meshkov interface,” *Phys. Fluids* **15**, 3730 (2003).
- ¹⁷ P. E. Dimotakis, “The mixing transition in turbulent flows,” *J. Fluid Mech.* **409**, 69 (2000).
- ¹⁸ K. O. Mikaelian, “Numerical simulations of Richtmyer-Meshkov instabilities in finite-thickness fluid layers,” *Phys. Fluids* **8**, 1269 (1996).
- ¹⁹ O. Sadot, L. Erez, G. Oron, G. Ben-Dor, U. Alon, L. A. Levin, and D. Shvarts, “Studies on the nonlinear evolution of the Richtmyer-Meshkov instability,” *Astrophys. J. Suppl.* **127**, 469 (2000).
- ²⁰ J. W. Jacobs, M. A. Jones, and C. E. Niederhaus, “Experimental studies of Richtmyer-Meshkov instability,” in *Proceedings of the Fifth International Workshop on Compressible Turbulent Mixing*, edited by R. Young, J. Glimm, and B. Boston (World Scientific, New York, 1996), pp.

195–202.

- ²¹ C. E. Niederhaus and J. W. Jacobs, “Experimental study of the Richtmyer-Meshkov instability of incompressible fluids,” *J. Fluid Mech.* **485**, 243 (2003).
- ²² A. D. Kotelnikov and N. J. Zabusky, “Vortex dynamics of a twice-accelerated interface in an incompressible ideal fluid,” *Astrophys. J. Suppl.* **127**, 389 (2000).
- ²³ A. D. Kotelnikov, J. Ray, and N. J. Zabusky, “Vortex morphologies on reaccelerated interfaces: Visualization, quantification and modeling of one- and two-mode compressible and incompressible environments,” *Phys. Fluids* **12**, 3245 (2000).
- ²⁴ J. W. Jacobs, D. G. Jenkins, D. L. Klein, and R. F. Benjamin, “Nonlinear growth of the shock-accelerated instability of a thin fluid layer,” *J. Fluid Mech.* **295**, 23 (1995).
- ²⁵ P. M. Rightley, P. Vorobieff, and R. F. Benjamin, “Evolution of a shock-accelerated thin fluid layer,” *Phys. Fluids* **9**, 1770 (1997).
- ²⁶ K. Kremeyer, S. Nazarenko, and A. C. Newell, “Shock bowing and vorticity dynamics during propagation into different transverse density profiles,” *Physica D* **163**, 150 (2002).
- ²⁷ S. Zhang, N. J. Zabusky, G. Peng, and S. Gupta, “Shock gaseous cylinder interactions: Dynamically validated initial conditions provide excellent agreement between experiments and numerical simulations to late–intermediate time,” *Phys. Fluids* **16**, 1203 (2004).
- ²⁸ C. B. Laney, *Computational Gasdynamics* (Cambridge University Press, New York, 1998).
- ²⁹ R. J. Leveque, *Finite Volume Methods for Hyperbolic Problems*, Cambridge Texts in Applied Mathematics (Cambridge University Press, New York, 2002).
- ³⁰ A. J. Chorin and J. E. Marsden, *A Mathematical Introduction to Fluid Mechanics*, vol. 4 of *Texts in Applied Mathematics* (Springer-Verlag, New York, 1993), 3rd ed.
- ³¹ J. P. Boris, F. F. Grinstein, E. S. Oran, and R. L. Kolbe, “New insights into large eddy simulation,” *Fluid Dyn. Res.* **10**, 199 (1992).
- ³² D. Drikakis, “Advances in turbulent flow computations using high-resolution methods,” *Prog. Aero. Sci.* **39**, 405 (2003).
- ³³ D. Balsara and C.-W. Shu, “Monotonicity preserving weighted essentially non-oscillatory schemes with increasingly high order of accuracy,” *J. Comput. Phys.* **160**, 405 (2000).
- ³⁴ C.-W. Shu, “High order ENO and WENO schemes for computational fluid dynamics,” in *High-Order Methods for Computational Physics*, edited by T. J. Barth and H. Deconinck (Springer-Verlag, New York, 1999), pp. 439–582.

- ³⁵ S. Karni, “Multicomponent flow calculations by a consistent primitive algorithm,” *J. Comput. Phys.* **112**, 31 (1994).
- ³⁶ S. Karni, “Hybrid multifluid algorithms,” *SIAM J. Sci. Comput.* **17**, 1019 (1996).
- ³⁷ R. Abgrall, “How to prevent pressure oscillations in multicomponent flow calculations: a quasi-conservative approach,” *J. Comput. Phys.* **125**, 150 (1996).
- ³⁸ R. Abgrall and S. Karni, “Computations of compressible multifluids,” *J. Comput. Phys.* **169**, 594 (2001).
- ³⁹ C.-W. Shu and S. Osher, “Efficient implementation of essentially nonoscillatory shock-capturing schemes,” *J. Comput. Phys.* **77**, 439 (1988).
- ⁴⁰ M. A. Jones and J. W. Jacobs, “A membraneless experiment for the study of Richtmyer-Meshkov instability of a shock-accelerated gas interface,” *Phys. Fluids* **9**, 3078 (1997).
- ⁴¹ J. W. Jacobs and V. V. Krivets, “Experiments on the late-time development of single-mode Richtmyer-Meshkov instability,” *Phys. Fluids* **17**, 034104 (2005).
- ⁴² G. I. Taylor, “The instability of liquid surfaces when accelerated in a direction perpendicular to their planes,” *Proc. R. Soc. Lond. A* **201**, 192 (1950).
- ⁴³ K. A. Meyer and P. J. Blewett, “Numerical investigation of the stability of a shock accelerated interface between two fluids,” *Phys. Fluids* **15**, 753 (1972).
- ⁴⁴ G. Fraley, “Rayleigh-Taylor stability for a normal shockwave-density discontinuity interaction,” *Phys. Fluids* **29**, 376 (1986).
- ⁴⁵ K. O. Mikaelian, “Freeze-out and the effect of compressibility in the Richtmyer-Meshkov instability,” *Phys. Fluids* **6**, 356 (1994).
- ⁴⁶ M. Vandenboomgaerde, C. Mügler, and S. Gauthier, “Impulsive model for the Richtmyer-Meshkov instability,” *Phys. Rev. E* **58**, 1874 (1998).
- ⁴⁷ K. O. Mikaelian, “Density gradient stabilization of the Richtmyer-Meshkov instability,” *Phys. Fluids A* **3**, 2638 (1991).
- ⁴⁸ R. E. Duff, F. H. Harlow, and C. W. Hirt, “Effects of diffusion on interface instability between gases,” *Phys. Fluids* **5**, 417 (1962).
- ⁴⁹ Q. Zhang and S. Sohn, “Non-linear theory of unstable fluid mixing driven by shock wave,” *Phys. Fluids* **9**, 1106 (1997).
- ⁵⁰ M. Vandenboomgaerde, S. Gauthier, and C. Mügler, “Nonlinear regime of a multimode Richtmyer-Meshkov instability: a simplified perturbation theory,” *Phys. Fluids* **14**, 1111 (2002).

- ⁵¹ C. Matsuoka, K. Nishihara, and Y. Fukuda, “Nonlinear evolution of an interface in the Richtmyer-Meshkov instability,” *Phys. Rev. E* **67**, 036301 (2003), erratum *Phys. Rev. E* **68**, 029902-1 (2003).
- ⁵² O. Sadot, L. Erez, U. Alon, D. Oron, and L. A. Levin, “Study of nonlinear evolution of single-mode and two bubble interaction under Richtmyer-Meshkov instability,” *Phys. Rev. Lett.* **80**, 1654 (1998).
- ⁵³ D. Layzer, “On the instability of superposed fluids in a gravitational field,” *Astrophys. J.* **122**, 1 (1955).
- ⁵⁴ V. N. Goncharov, “Analytical model of nonlinear, single-mode, classical Rayleigh-Taylor instability at arbitrary Atwood numbers,” *Phys. Rev. Lett.* **88**, 134501 (2002).
- ⁵⁵ S.-I. Sohn, “Simple potential-flow model of Rayleigh-Taylor and Richtmyer-Meshkov instabilities for all density ratios,” *Phys. Rev. E* **67**, 026301 (2003).
- ⁵⁶ S.-I. Sohn, “Density dependence of a Zuffria-type model for Rayleigh-Taylor bubble fronts,” *Phys. Rev. E* **70**, 045301 (2004).
- ⁵⁷ J. A. Zuffria, “Bubble competition in Rayleigh-Taylor instability,” *Phys. Fluids* **31**, 440 (1988).
- ⁵⁸ S.-I. Sohn and Q. Zhang, “Late time behavior of bubbles at unstable interfaces in two dimensions,” *Phys. Fluids* **13**, 3493 (2001).
- ⁵⁹ K. O. Mikaelian, “Explicit expressions for the single-mode Rayleigh-Taylor and Richtmyer-Meshkov instabilities at arbitrary Atwood numbers,” *Phys. Rev. E* **67**, 026319 (2003).
- ⁶⁰ H. M. Antia, *Numerical Methods for Scientists and Engineers* (Birkäuser, Boston, 2002).
- ⁶¹ A. W. Cook and P. E. Dimotakis, “Transition stages of Rayleigh-Taylor instability between miscible fluids,” *J. Fluid Mech.* **443**, 69 (2001), corrigendum, *J. Fluid Mech.* **457** (2002), 410.
- ⁶² L. F. Henderson, “On the refraction of shock waves,” *J. Fluid Mech.* **198**, 365 (1989).
- ⁶³ K. Sinha and G. V. Candler, “Turbulent dissipation-rate equation for compressible flows,” *AIAA J.* **41**, 1017 (2003).
- ⁶⁴ S. Pirozzoli, F. Grasso, and T. B. Gatski, “Direct numerical simulation and analysis of a spatially evolving supersonic turbulent boundary layer at $M = 2.25$,” *Phys. Fluids* **16**, 530 (2004).
- ⁶⁵ J. A. Ekaterinaris, “Performance of high-order-accurate, low-diffusion numerical schemes for compressible flow,” *AIAA J.* **42**, 493 (2004).
- ⁶⁶ J. A. Ekaterinaris, “High-order accurate, low numerical diffusion methods for aerodynamics,” *Prog. Aero. Sci.* **41**, 192 (2005).

- ⁶⁷ T. S. Cheng and K. S. Lee, “Numerical simulations of underexpanded supersonic jet and free shear layer using WENO schemes,” *Int. J. Heat and Fluid Flow* **26**, 755 (2005).
- ⁶⁸ B. Costa, W. S. Don, D. Gottlieb, and R. Sendersky, “Two-dimensional multi-domain hybrid spectral-WENO methods for conservation laws,” *Commun. Comput. Phys.* **1**, 548 (2006).

Figures

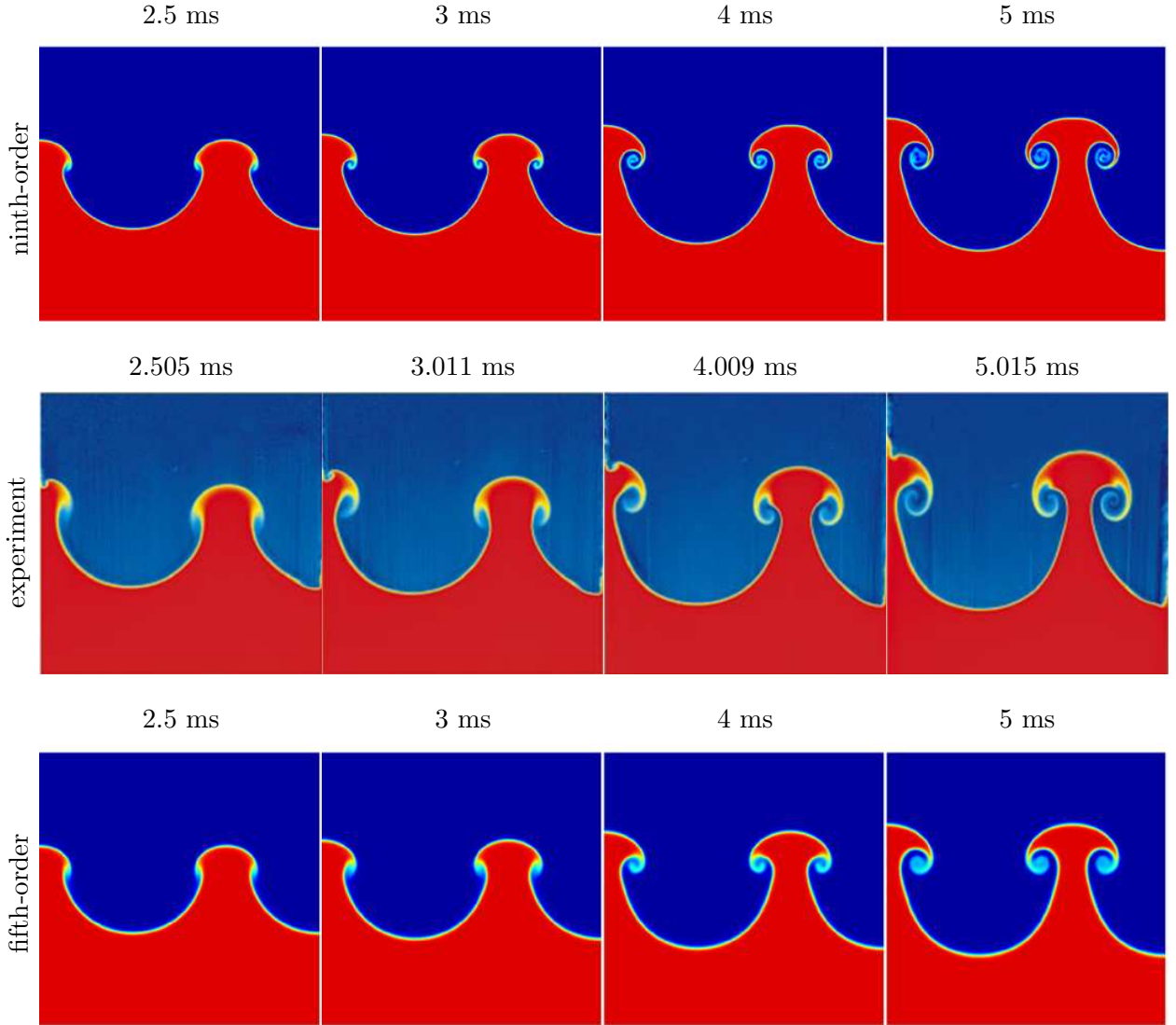


FIG. 1: (Color). Comparison of corrected PLIF images from the experiment of Collins and Jacobs¹⁵ (middle row) with the density from the ninth-order WENO simulation (top row) and from the fifth-order WENO simulation (bottom row) at selected times before reshock. The gases are air(acetone) (blue) and SF_6 (red). The simulation times differ slightly from the experimental times by 0.005–0.015 ms. The experimental images are taken from Fig. 6 of Collins and Jacobs (reprinted with the permission of Cambridge University Press).

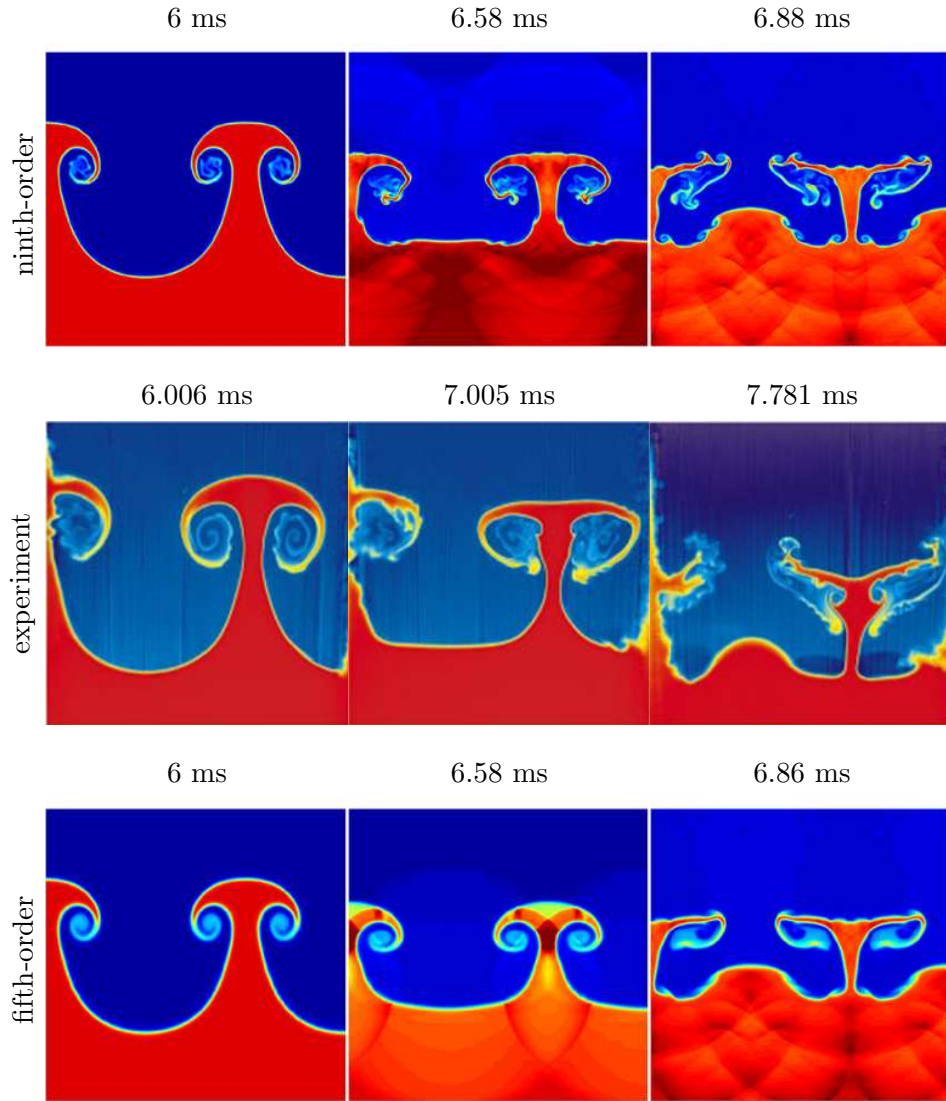


FIG. 2: (Color). Further comparison of corrected PLIF images from the experiment of Collins and Jacobs¹⁵ and the density from the fifth- and ninth-order WENO simulations at selected times just before and after reshock of the evolving interface. The experimental images are taken from Fig. 6 of Collins and Jacobs (reprinted with the permission of Cambridge University Press).

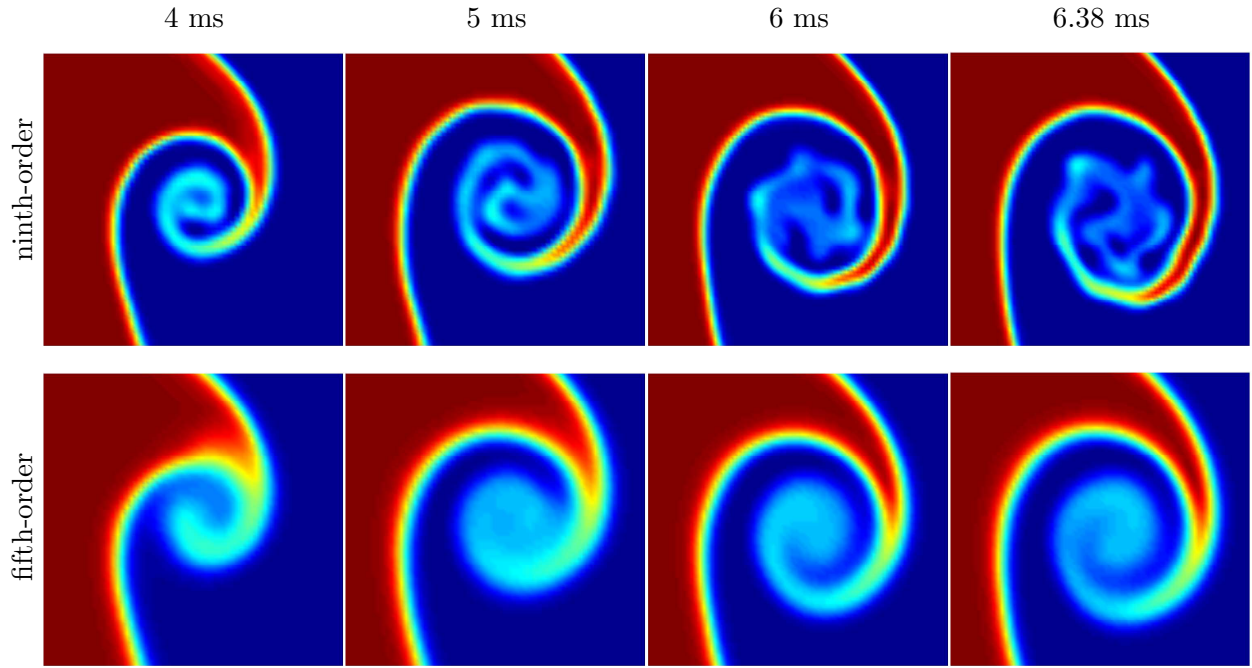


FIG. 3: (Color). Details of the roll-up in the density field, ρ , from the ninth-order (top row) and fifth-order (bottom row) WENO simulations at 4, 5, 6 and 6.38 ms.

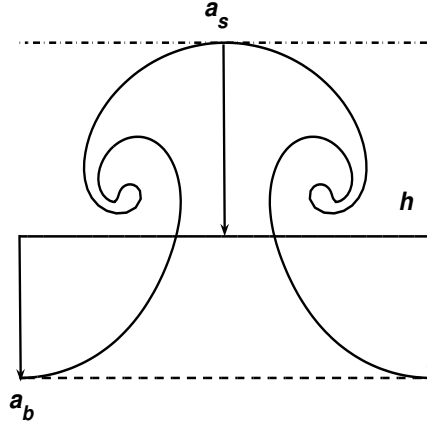


FIG. 4: A typical interface evolving according to the single-mode Richtmyer-Meshkov instability with bubble and spike amplitudes a_b and a_s , and mixing layer width h (the image is from a point vortex simulation). The solid line in the center is the location of the shocked unperturbed interface, and is used as the reference to measure the bubble and spike amplitudes. The mixing layer width is $h = a_b + a_s$ and the amplitude is $a = (a_b + a_s)/2$. The bubble and spike velocities considered later are given by $v_b = da_b/dt$ and $v_s = da_s/dt$, respectively.

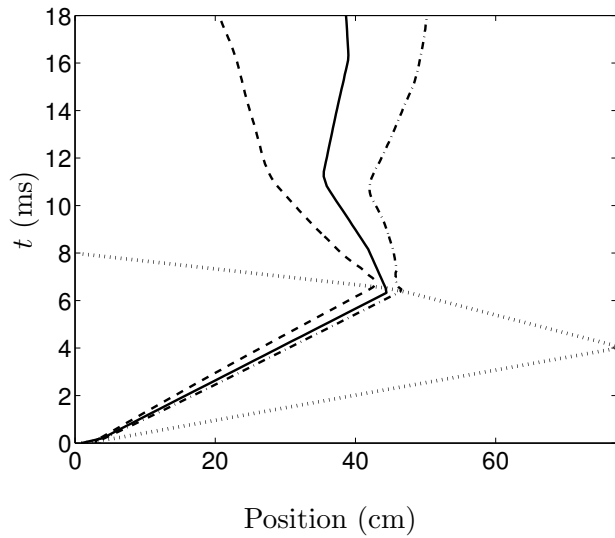


FIG. 5: The x - t diagram showing the position of the interface $\ell_{\text{int}}(t)$ (solid line), shock (dotted line), and bubble and spike tip locations $\ell_b(t)$ and $\ell_s(t)$ (dash-dot and dashed lines, respectively) from the ninth-order simulation. The horizontal distance between the spike and bubble tip location is the mixing layer width $h(t)$.

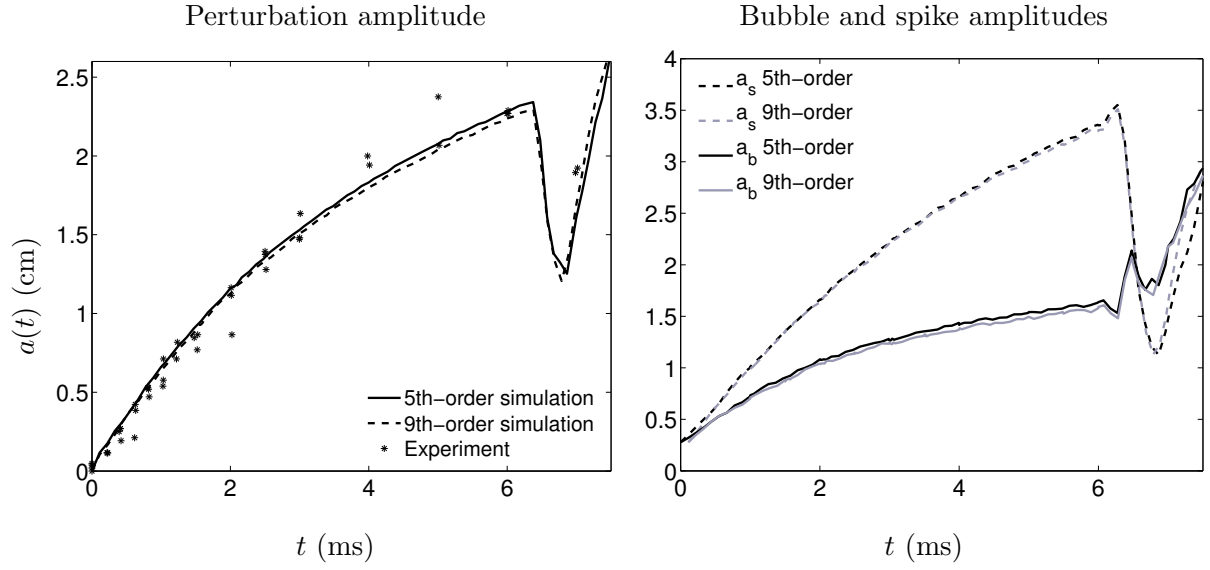


FIG. 6: Comparison of the amplitude obtained from the fifth- and ninth-order WENO simulation to the experimental data points from Collins and Jacobs¹⁵ (left). The bubble and spike amplitudes from the simulations, $a_b(t)$ and $a_s(t)$, respectively, are also shown (right).

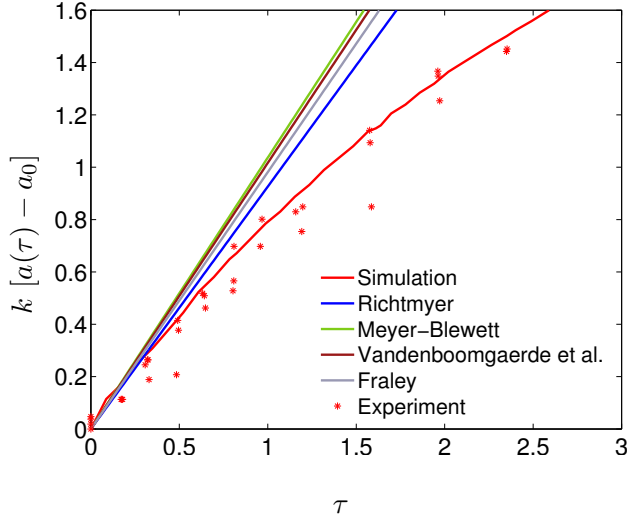


FIG. 7: (Color). The normalized amplitude $k[a(\tau) - a_0]$ versus τ from the ninth-order WENO simulation and the experimental data points, together with the predictions of the impulsive models. The Richtmyer model gives the smallest slope ($da/dt = 740.1$ cm/s) as it uses the post-shock Atwood number and amplitude. The pre- and post-shock amplitudes are averaged in the Meyer-Blewett model, resulting in the largest slope, 828.6 cm/s. The pre- and post-shock amplitudes are averaged by the pre- and post-shock Atwood numbers, respectively, in the Vandenboomgaerde *et al.* model which thus, predicts a slightly smaller slope, 812.4 cm/s, than that predicted by the Meyer-Blewett model, but larger than the slope predicted by the Richtmyer model. The Fraley model has an exact initial slope of 784.3 cm/s, intermediate between those predicted by the Meyer-Blewett and Vandenboomgaerde *et al.* models.

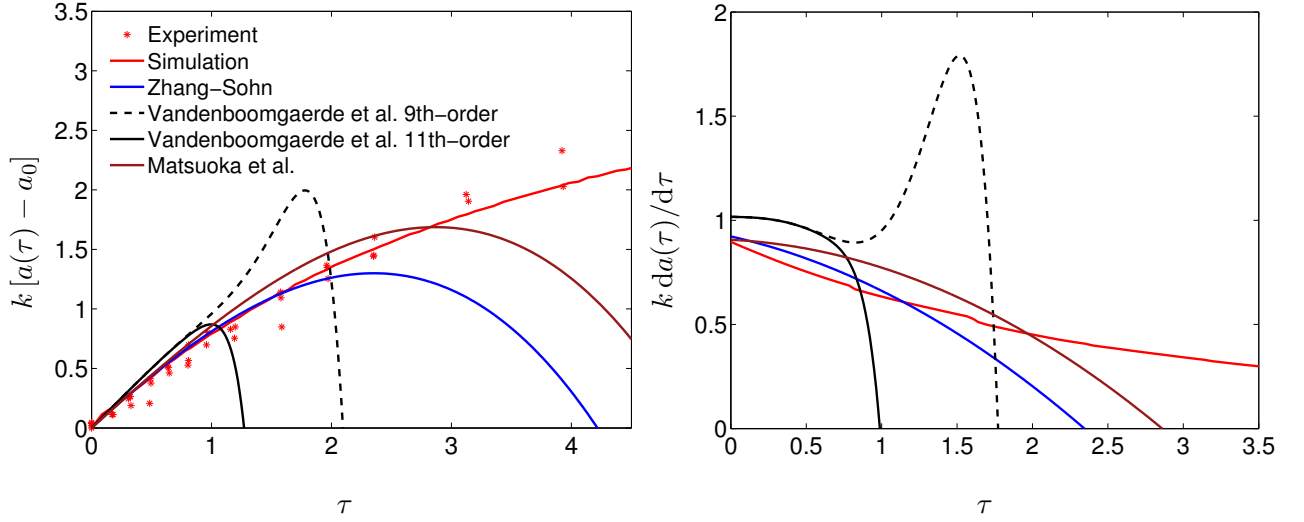


FIG. 8: (Color). The normalized amplitude $k[a(\tau) - a_0]$ versus τ from the ninth-order WENO simulation and the experimental data points, together with the predictions of the Zhang-Sohn, Vandenboomgaerde *et al.* and Matsuoka *et al.* perturbation series models (left). The normalized growth rates $k da(\tau)/d\tau$ versus τ from the ninth-order simulation, together with the corresponding growth rates from the perturbation series models, are also shown (right).

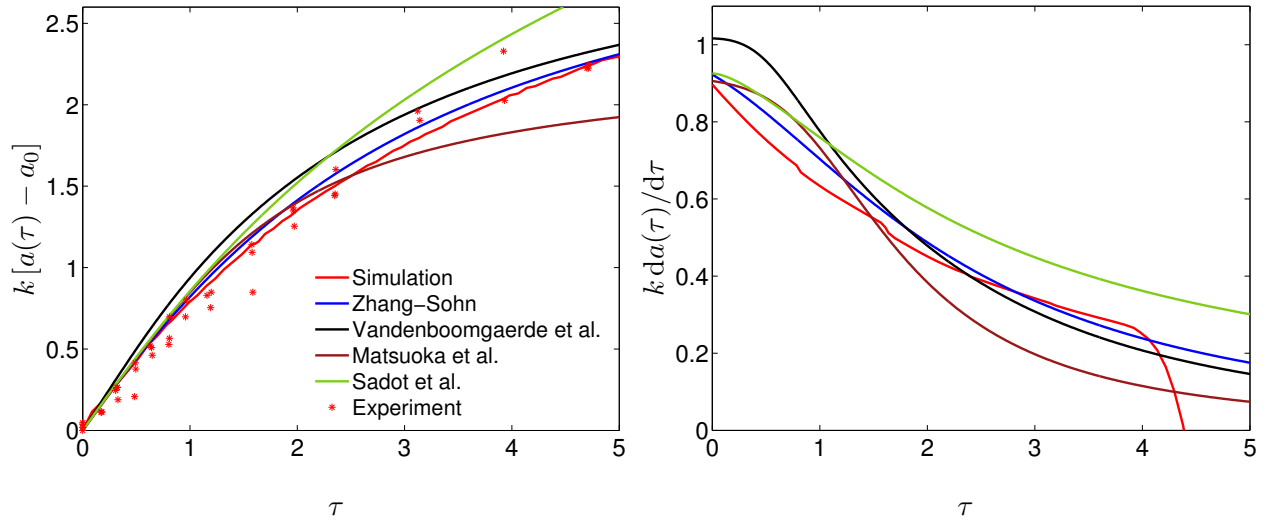


FIG. 9: (Color). The normalized amplitude $k[a(\tau) - a_0]$ versus τ from the ninth-order WENO simulation and the experimental data points, together with the predictions of the Zhang-Sohn, Vandenboomgaerde *et al.* and Matsuoka *et al.* models extended via Padé approximants, and the Sadot *et al.* model (left). The normalized growth rates $k da(\tau)/d\tau$ versus τ from the ninth-order simulation, together with the corresponding growth rates from the nonlinear models extended via Padé approximants, are also shown (right).

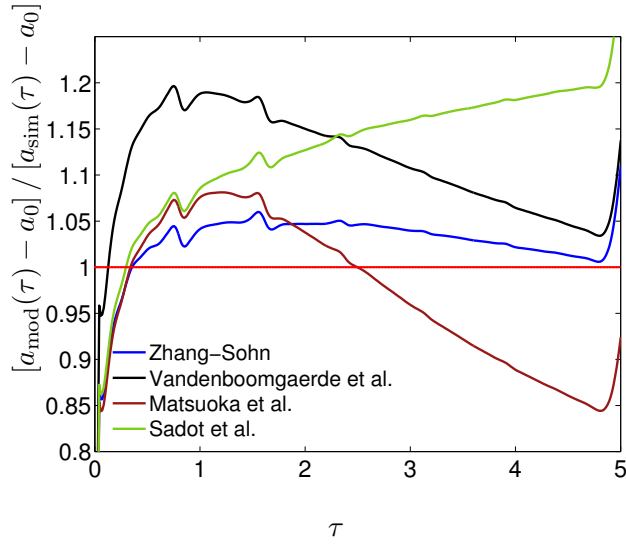


FIG. 10: (Color). The predictions of the Zhang-Sohn (Padé), Vandenboomgaerde *et al.* (Padé), Matsuoka *et al.* (Padé) and Sadot *et al.* models (with the initial perturbation amplitude subtracted out) divided by the corresponding ninth-order WENO simulation amplitude.

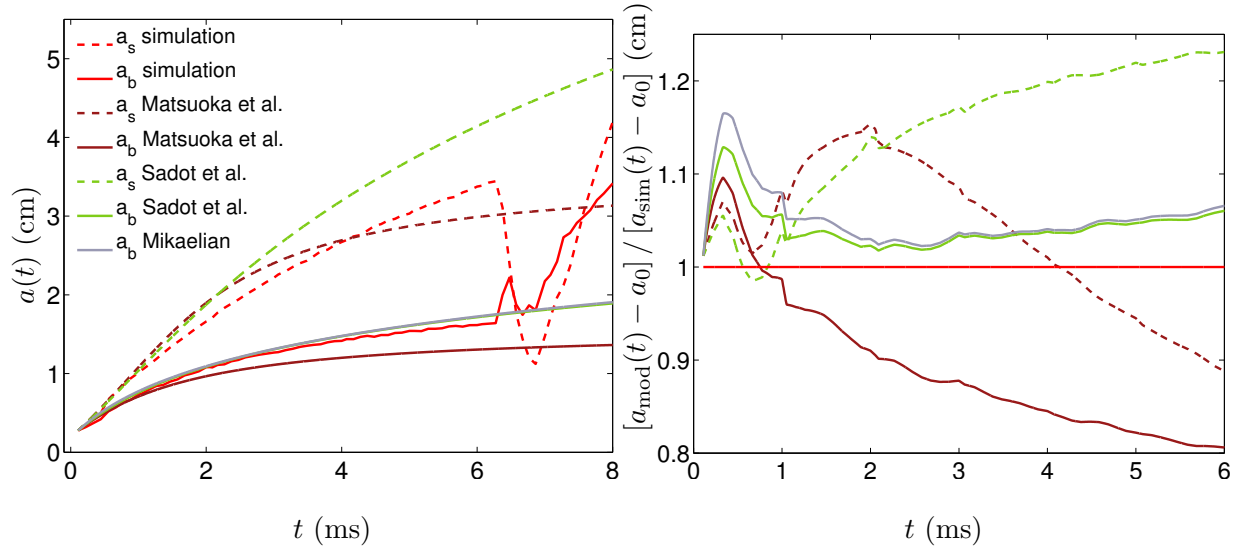


FIG. 11: (Color). Comparison of the bubble and spike amplitudes, $a_b(t)$ and $a_s(t)$, from the ninth-order WENO simulation with the predictions of the Matsuoka *et al.* (Padé) and Sadot *et al.* models, and with the Mikaelian model in the case of the bubble amplitude (left). Also shown are the ratios of the model predictions to the simulation bubble and spike amplitudes (with the initial perturbation amplitude subtracted out) (right).

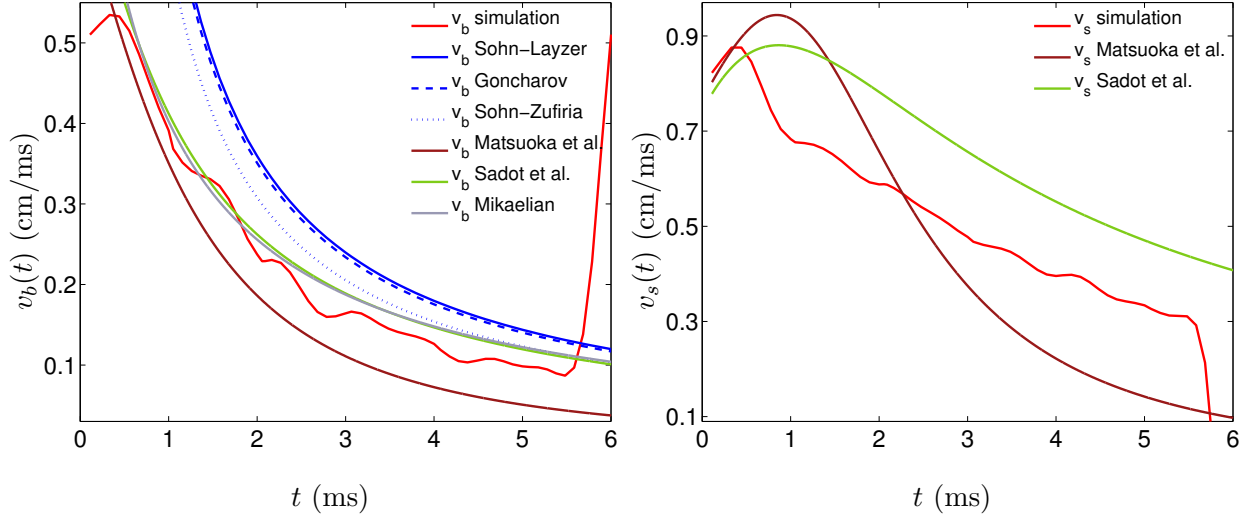


FIG. 12: (Color). The bubble velocity, $v_b(t)$, from the ninth-order WENO simulation with the asymptotic velocities predicted by the Goncharov, Sohn-Layzer and Sohn-Zufiria models and the velocities predicted by the Matsuoka *et al.*, Sadot *et al.* and Mikaelian models (left). Also shown is the spike velocity, $v_s(t)$, and the velocities predicted by the Matsuoka *et al.* and Sadot *et al.* models (right).

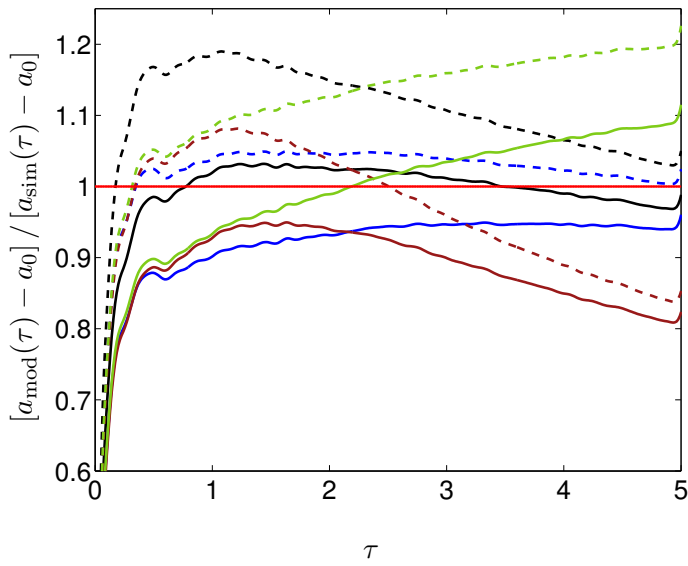
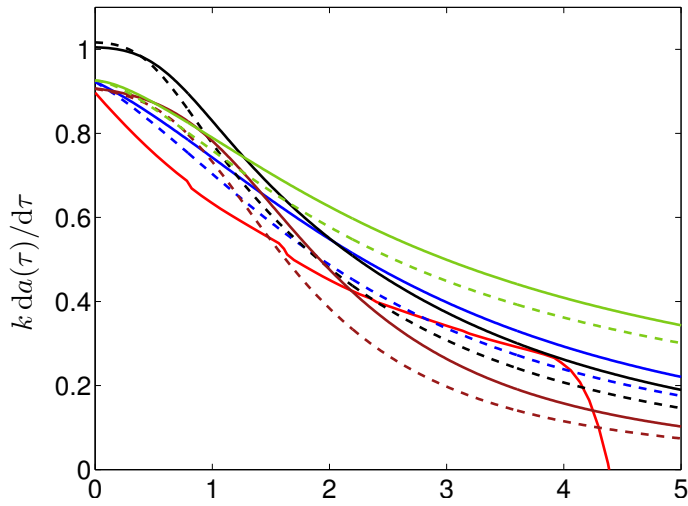
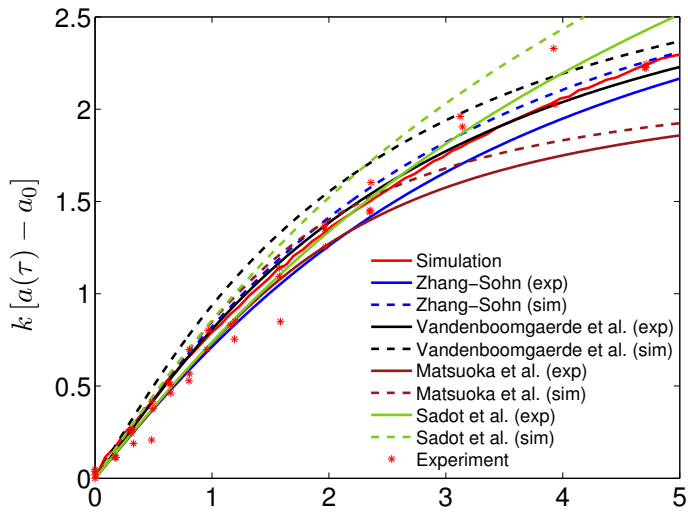


FIG. 13: (Color). The normalized amplitude predictions (with the initial perturbation amplitude subtracted out) of the nonlinear models using the experimental and simulation parameters v_0 , A^+ , a_0^+ and Δu (as given in Table II), together with the experimental data points and the ninth-order WENO simulation data (top). The normalized amplitude growth rate predictions of the nonlinear models with the experimental and simulation parameters, together with the ninth-order simulation data, are also shown (middle). Also shown are the ratios of the model predictions to the simulation data (bottom).

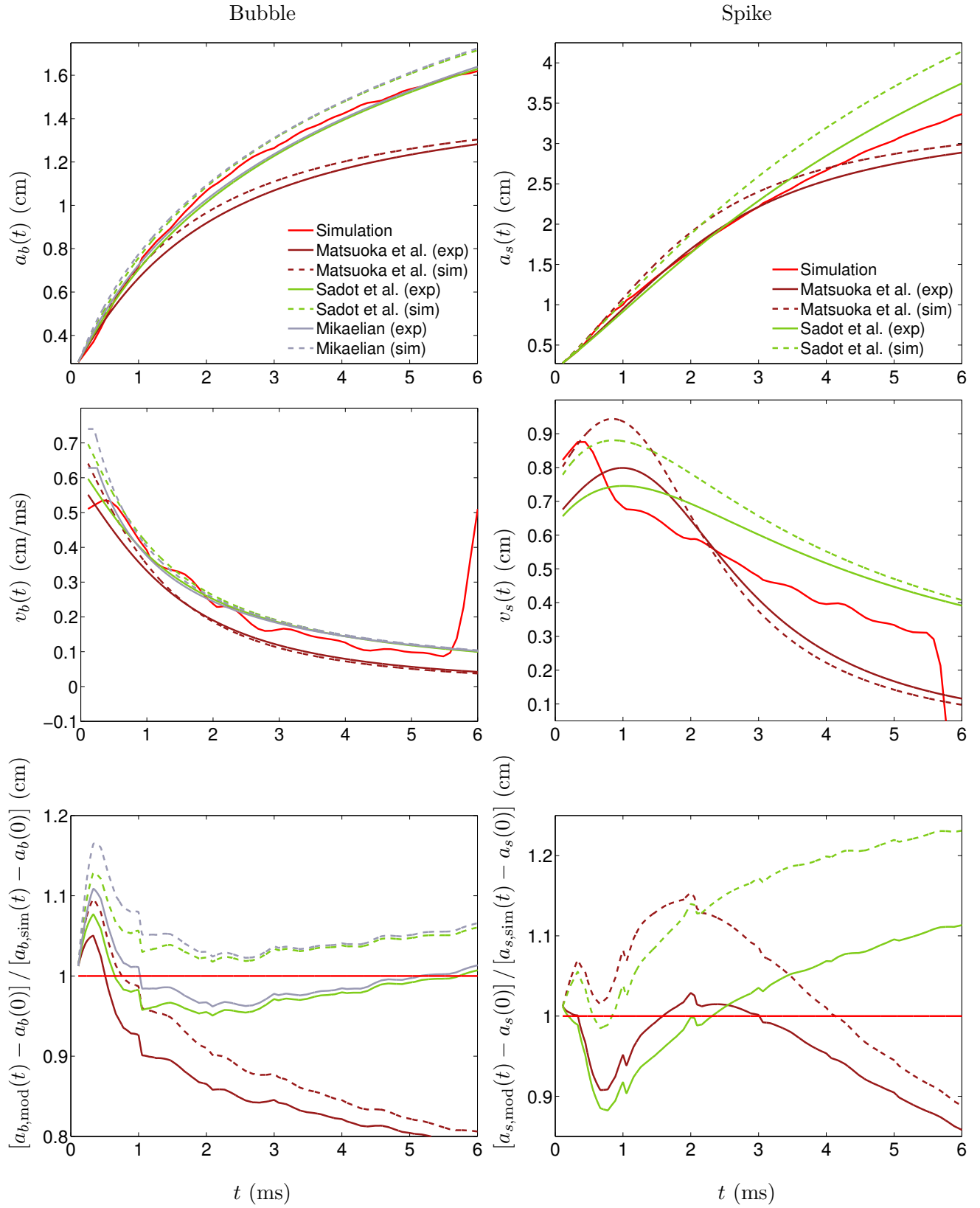


FIG. 14: (Color). The predictions for the bubble amplitude, bubble velocity, and ratio of the model predictions (with the initial perturbation amplitude subtracted out) to the ninth-order WENO simulation results, using the experimental and simulation parameters v_0 , A^+ , a_0^+ and Δu (as given in Table II) (left). The predictions for the spike amplitude, spike velocity, and ratio of the model predictions to the simulation results, using the experimental and simulation parameters is also shown (right).

Tables

	Single-gamma (simulation) value		Two-gamma value	
γ_{aa}	1.276		1.276	
γ_{SF_6}	1.276		1.093	
M_{aa} (g/mol)	34.76		34.76	
M_{SF_6} (g/mol)	146.05		146.05	
$u_{i,shock}$ (cm/s)	36369		36369	
$u_{r,shock}$ (cm/s)	33473		33301	
$u_{t,shock}$ (cm/s)	19218		17945	
$t_{reshock}$ (ms)	6.36		6.61	
	Pre-shock	Post-shock	Pre-shock	Post-shock
ρ_{aa} (g/cm ³)	1.351×10^{-3}	2.084×10^{-3}	1.351×10^{-3}	2.065×10^{-3}
ρ_{SF_6} (g/cm ³)	5.494×10^{-3}	8.456×10^{-3}	5.494×10^{-3}	9.021×10^{-3}
A	0.6053	0.6045	0.6053	0.6274
p (bar)	0.956	1.667	0.956	1.648
T_{aa} (K)	296	334.4	296	333.6
T_{SF_6} (K)	305	346	305	321

TABLE I: The pre- and post-shock state [adiabatic exponents γ_r , molecular weights M_r , incident, reflected and transmitted shock speeds $u_{i,shock}$, $u_{r,shock}$ and $u_{t,shock}$, densities ρ_r , Atwood number $A = (\rho_{SF_6} - \rho_{aa})/(\rho_{SF_6} + \rho_{aa})$, pressure p , and temperatures T_r ($r = 1, 2$)] of the air(acetone) and SF₆ gases from one-dimensional shock refraction theory. The simulation (single-gamma) values were obtained assuming $\gamma = 1.276$ and the two-gamma values were obtained using $\gamma_1 = 1.276$ and $\gamma_2 = 1.093$, corresponding to the air(acetone) mixture and the SF₆, respectively. The time of reshock, $t_{reshock}$, is also indicated.

	Simulation value		Experimental value	
Δu (cm/s)	6731		6060	
v_0 (cm/s)	702		628	
η_{comp}	0.8071		–	
	Pre-shock	Post-shock	Pre-shock	Post-shock
a_0 (cm)	0.2	0.162	0.183	0.157
A	0.6053	0.6045	0.604	0.625
ψ	1.17	1.08	1.17	1.08

TABLE II: The interface velocity Δu and Richtmyer velocity v_0 from the ninth-order simulation and experiment. The pre- and post-shock values of the perturbation amplitude a_0 , Atwood number A and growth reduction factor ψ obtained from one-dimensional shock refraction theory are also compared to the values reported by Collins and Jacobs.¹⁵

	$\Delta_{\text{exp}} (\%)$	$\Delta_{\text{sim}} (\%)$
Zhang-Sohn Padé	6.8	3.3
Vandenboomgaerde et al. Padé	1.9	10.1
Matsuoka et al. Padé (all)	12	8.1
Matsuoka et al. Padé (bubble)	26.4	20.4
Matsuoka et al. Padé (spike)	9.1	15.9
Sadot et al. (all)	4.5	12.8
Sadot et al. (bubble)	3.7	4.5
Sadot et al. (spike)	16.8	26.6
Mikaelian (bubble)	2.6	5.2

	$\Delta_{\text{exp}}^e (\%)$	$\Delta_{\text{sim}}^e (\%)$
Zhang-Sohn Padé	9.9	11.4
Vandenboomgaerde et al. Padé	11.7	14.3
Matsuoka et al. Padé	8.4	15.6
Sadot et al.	10.1	19.2

TABLE III: Average fractional deviation between the simulation amplitude $a_{\text{sim}}(t)$ and the model prediction $a_{\text{mod}}(t)$ when experimental parameters are used (Δ_{exp}) and when the simulation parameters are used (Δ_{sim}). Also shown are the average fractional deviation between the experimental amplitude $a_{\text{exp}}(t)$ and the model prediction $a_{\text{mod}}(t)$ when the experimental parameters are used (Δ_{exp}^e) and when the simulation parameters are used (Δ_{sim}^e).